

DEUTSCHES ELEKTRONEN-SYNCHROTRON

Ein Forschungszentrum der Helmholtz-Gemeinschaft

DESY 11-134

August 2011

Scheme for generating and transporting THz radiation to the X-ray experimental floor at the LCLS baseline

Gianluca Geloni,
European XFEL GmbH, Hamburg

Vitali Kocharyan and Evgeni Saldin
Deutsches Elektronen-Synchrotron DESY, Hamburg

ISSN 0418-9833

NOTKESTRASSE 85 - 22607 HAMBURG

Scheme for generating and transporting THz radiation to the X-ray experimental floor at the LCLS baseline

Gianluca Geloni,^{a,1} Vitali Kocharyan^b and Evgeni Saldin^b

^a*European XFEL GmbH, Hamburg, Germany*

^b*Deutsches Elektronen-Synchrotron (DESY), Hamburg, Germany*

Abstract

This paper describes a novel scheme for integrating a coherent THz source in the baseline of the LCLS facility. Any method relying on the spent electron beam downstream of the baseline undulator should provide a way of transporting the radiation up to the experimental floor. Here we propose to use the dump area access maze. In this way the THz output must propagate with limited size at least for one hundred meters in a maze, following many turns, to reach the near experimental hall. The use of a standard, discrete, open beam-waveguide formed by periodic reflectors, that is a mirror guide, would lead to unacceptable size of the system. To avoid these problems, in this paper we propose an alternative approach based on periodically spaced metallic screens with holes. This quasi-optical transmission line is referred to as an iris line. We present complete calculations for the iris line using both analytical and numerical methods, which we find in good agreement. We present a design of a THz edge radiation source based on the use of an iris line. The proposed setup takes almost no cost nor time to be implemented at the LCLS baseline, and can be used at other facilities as well. The edge radiation source is limited in maximally achievable field strength at the sample. An extension based on the use of an undulator in the presence of the iris line, which is feasible at the LCLS energies, is proposed as a possible upgrade of the baseline THz source.

1 Introduction

The accelerator complex at the LCLS produces ultra-short electron bunches approaching sub-hundred fs duration. It is natural to take advantage of

¹ Corresponding Author. E-mail address: gianluca.geloni@xfel.eu

these ultra-short bunches in order to provide coherent THz radiation [1]. In fact, intense, coherent THz radiation pulses can be produced from the sub-hundred fs electron bunches at wavelength longer than, or comparable with the bunch length, leading to radiated energy levels proportional to the square of the electron number, in contrast to the incoherent case when energy in the radiation pulse scales linearly with the number of electrons involved in the process. The result is an enhancement in radiation intensity of up to 9 – 10 orders of magnitude.

The exploitation of such kind of coherent THz source as a part of the LCLS-II baseline user facility has been proposed in the LCLS-II Conceptual design report [1]. THz radiation pulses can be generated by the spent electron beam downstream of the X-ray undulator. In this way, intrinsic synchronization with the X-ray pulses can be achieved. A first, natural application of this kind of the photon beams is for pump-probe experiments. Through the combination of THz pump and X-ray probe, LCLS-II would offer unique opportunities for studies of ultrafast surface chemistry and catalysis [1]. Also, the LCLS team started an *R&D* project on THz radiation from the spent electron beam downstream of the undulator [2]. The THz is generated by inserting a thin Be foil into the electron beam [3]. In this paper we describe a novel scheme for integrating such kind of source in the baseline of the LCLS facility.

The transport of the THz radiation from the LCLS beam dump area to the near experimental hall constitutes a challenge. A major constraint for the LCLS baseline case is constituted by the upstream shielding wall and by the Far End Enclosure (FEE) downbeam shielding wall. It follows that transport of the THz beam can only be achieved using the dump area access maze, and relying on a limited size [4, 5]. However, in this way, the THz output must propagate at least 100 meters to reach the near experimental hall. Since THz beams are prone to significant diffraction, a suitable beam transport system must be provided to guide the beam along large distances maintaining it, at the same time, within a reasonable size. Moreover, the THz beamline should be designed to obtain a large transmission efficiency for radiation over a wide wavelength range. Usually, the focusing of the THz beam can only be achieved with reflective optics because lenses made from any material would reflect and absorb all radiation. In order to cope with the unacceptable size increase, in this paper we propose an alternative solution to a mirror guide, based on the use of periodically spaced metallic screens with holes. This quasi-optical transmission line is referred to as an iris line, or an iris beam waveguide. The eigenmodes of the iris line have been calculated numerically for the first time by Fox and Li [6] and later obtained analytically by Vainstein [7, 8]. When the Fresnel number of the iris line is large, eigenmodes are characterized by rather small diffraction losses. For instance, at a wavelength $\lambda \sim 0.1$ mm, for an iris radius $a \sim 5$ cm, and

for a the distance between the iris $b \sim 30$ cm, the Fresnel number is given by $a^2/(\lambda b) \sim 10^2$, and diffraction losses of the principal eigenmode are found to be about 10% in 100 meters. Also, the iris line is rather stable with respect to screens misalignments. When the screens are adjusted in transverse and longitudinal directions with an accuracy better than 1 mm, misalignment do not result in extra diffraction losses within the THz wavelength range.

In this paper we present complete iris line theory calculations. In particular, the iris line eigenmodes are studied. The analysis of the transmission line has been performed in two steps: the first one consists of numerical simulations employing the method by Fox and Li [6], the second one by analytical calculations using the method by Vainstein [7, 8]. Numerical simulation results are in good agreement with analytical results.

In order to efficiently couple radiation into the transmission line, it is desirable to match the spatial pattern of the source radiation to the mode of the transmission line. To this end, it is advisable to generate radiation from the spent electron beam directly in an iris line with the same parameters a and b used in transmission line. In this way, the source generates THz radiation pulses with a transverse mode that automatically matches the mode of the transmission line. We developed a theory supporting this choice of THz source. As for the microwave waveguide case, one can use a Green's function approach to solve the field equations. According to method by Vainstein [7], one can set complex boundary conditions for the field on the virtual side surface of the iris line, which are called impedance boundary conditions. The problem of an open waveguide excitation is thus reduced to that of a closed waveguide. Our consideration is quite general, and can be applied to edge radiation sources as well as to undulator radiation sources in the presence of an iris line.

We present a complete design for a THz edge radiation source at the LCLS baseline. It includes a 15 m-long electron beam vacuum chamber equipped with an iris line, and a 100 m-long transmission line with the same parameters. The transmission line, which develops through the access maze, presents six 90 degrees turns with plane mirrors at 45 degrees as functional components. It is possible to match incident and outgoing radiation without extra losses in these irregularities. The proposed setup takes almost no cost nor time to be implemented at the LCLS baseline.

The THz edge radiation source is limited concerning the achievable field strength. An optimal expansion strategy for the LCLS THz source would include a THz undulator source. Such modern, high power THz source is exemplified by devices such as the coherent THz undulator source at FLASH at DESY [9, 10]. In this paper we will describe this likely extension and its accommodation together with the proposed edge radiation source. Both

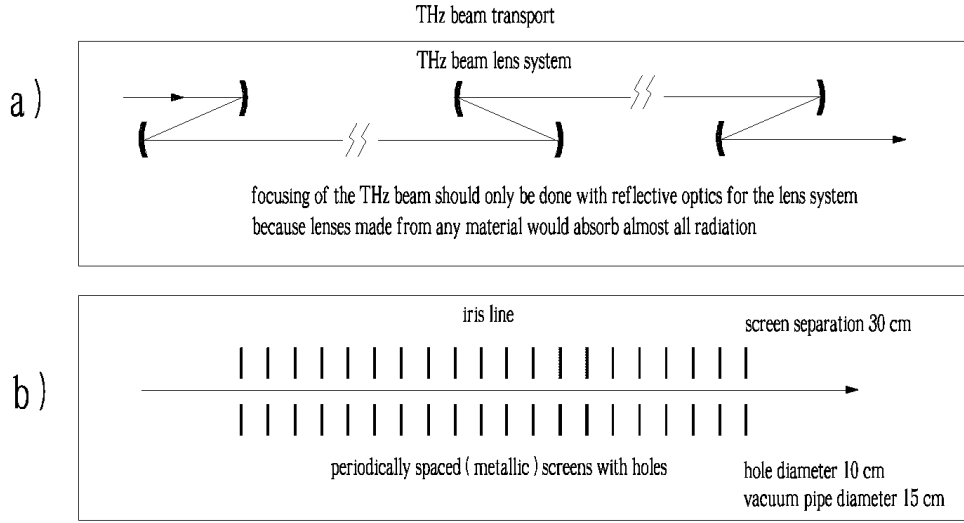


Fig. 1. Optical arrangement for the THz beam transport system. (a) THz beam lens system. Focusing of the THz beam can only be performed with reflective optics. In fact, lenses made of any material (except diamond) would absorb almost all radiation. (b) The use of an iris line, made of periodically spaced metallic screens with holes is a way to obtain a high transfer efficiency at small diameter of the beam pipe.

options have advantages, and disadvantages. The edge radiation source is characterized by low cost and can operate at all electron beam energies, but is limited in field strength. The THz undulator source would provide increase in field strength, but a trade-off must be reached between the far-infrared and the X-ray achievable frequency range due to technical limitations on magnetic field strength of room-temperature electromagnetic undulators ².

2 Principles of THz radiation generation based on the use of an iris line

2.1 Coherent THz edge radiation source

As discussed above, the availability of a THz source at XFEL facilities should be complemented by the availability of a suitable THz beam transport system, which must guide the beam for distances in the 100 meters range.

The THz beam can only be transmitted with quasi-optical techniques. In

² On the one hand, a decreased electron energy extends the far-infrared frequency range. On the other hand, it limits the X-ray frequency range.

particular, the idea of providing a periodic phase correction for the free-space beam, in order to compensate for its divergence, is very natural. In the 1960s numerous attempts of designing various quasi-optical transmission lines were reported. In particular, it was proposed to use open beam waveguides such as lens guides, mirror guides, and iris guides [6]-[17]. The competition among different proposals ended with the victory of mirror guides, still in use today e.g. for plasma heating [16, 17].

Focusing of the THz beam can only be provided with reflective optics since lenses made of any material would reflect and absorb all radiation at long distances³. Fig. 1 (a) shows the optical arrangement of a transport system based on the use of a mirror guide. Each focusing unit is composed by two matched copper mirrors. The mirrors are separated in such a way that the incident angle is sufficiently small to minimize astigmatism. Existing mirror guides are characterized by a maximal length of about 40 – 60 m [18, 19]. However, at XFEL facilities, scientists need a beam transport system working for significantly longer distances. The transverse size of the line is critical for this kind of applications of an open waveguide. Since at LCLS baseline the open guide should be installed within a maze with limiting size, advantages of the mirror guide are not evident.

In order to keep the transverse size of the guide to an acceptable level we propose, as an alternative to the mirror line solution, to use the iris line in Fig. 1 (b). Iris lines are characterized by a low attenuation of the fundamental mode, self-filtering of higher order modes, wide operational wavelength range and mechanical integrity of the structure. The first investigation of the influence of diffraction effects on the formation of the field eigenmodes in an iris line was carried out by Fox and Li using physical optics techniques [6]. According to their explanation, an iris line operates in the following way. Consider an electromagnetic wave passing inside the sequence of iris. When the wave diffracts at the first iris it produces a diffraction pattern in the plane of the next iris. If the second iris lets the main maximum of the diffraction pattern through, diffraction losses are minimal. Further on, sideband maxima of the diffraction pattern produced by the second iris are smaller than those in the first pattern. After the wave has passed a large number of irises, a field eigenmode is formed which has low diffraction losses.

A very different and mathematically solid approach to the same problem was introduced by Vainstein [7, 8]. His studies were based on direct solution of Maxwell equations. They showed that the way the electromagnetic field

³ In addition to absorption losses, a dielectric lens suffers from reflections at its boundaries as well. These surface reflections include a number of effects that are almost always harmful.

is confined inside an iris line, is essentially different from the guiding mechanism in stable lens guides or mirror guides. In fact, for iris guides, both diffraction and reflection from the iris edges are involved. An analysis of this effect allowed Vainstein to derive for the first time analytic expressions for field distribution and mode losses in iris guides. Complex boundary conditions are set on the virtual side surface of the iris line, the so called impedance boundary conditions, and the problem of an open waveguide transmission is therefore reduced to that of a closed waveguide. An iris line has distinct transverse modes. These eigenmodes are similar albeit not identical to microwave waveguide modes. For instance, one can find that iris line modes, in contrast with microwave waveguide modes, are independent of the polarization of the radiation.

An infinite discrete set of eigenfunctions with corresponding complex eigenvalues can be found. This set of modes comprises leaky modes which are non-orthogonal and non-normalizable with respect to the usual definition of inner product. To overcome this difficulty one can define a bilinear form which, for our purpose, is equivalent to an inner product under which modes are orthonormal. Bi-orthogonality is often exploited in different problems [11]. For example, it can be shown that the treatment of a microwave overmoded waveguide with resistive walls can be treated in terms of Leontovich impedance boundary conditions and of a bi-orthogonal set of eigenmodes, in formal analogy with those for a microwave waveguide with perfectly conducting walls. From the mathematical viewpoint, the iris guide theory with Vainstein boundary conditions is not fundamentally different from the theory of microwave waveguide with resistive walls.

As already mentioned, an iris line constitutes a suitable THz beam transport system for the LCLS baseline. Calculations indicate that the losses of the principal mode should be in the 10% level per 100 meters. The transfer line pipe radius is estimated to be equal to 7 cm. It is therefore technically feasible to install such transfer line inside the access maze. However, in order to efficiently couple radiation into transmission line, one also needs to match the spatial pattern of the source radiation to the mode of transmission line. First we analyze a coherent edge radiation source in the THz range, which is relatively simple to implement at XFELs. A setup where edge radiation is formed with the help of upstream and downstream metallic screens (foils) is shown in Fig. 2. The edge radiation from the upstream screen is extracted by the downstream metallic screen, which acts as a mirror, and is sent to the iris transmission line. The length of the straight section between upstream screen and mirror plays the role of the length of the insertion device for edge radiation⁴ [20]. The matching problem is easily solved if the THz

⁴ A hole may be present or not in the edge radiation screens. In the hard X-ray regime of operation Be foils without hole can be used. In the soft X-ray regime the

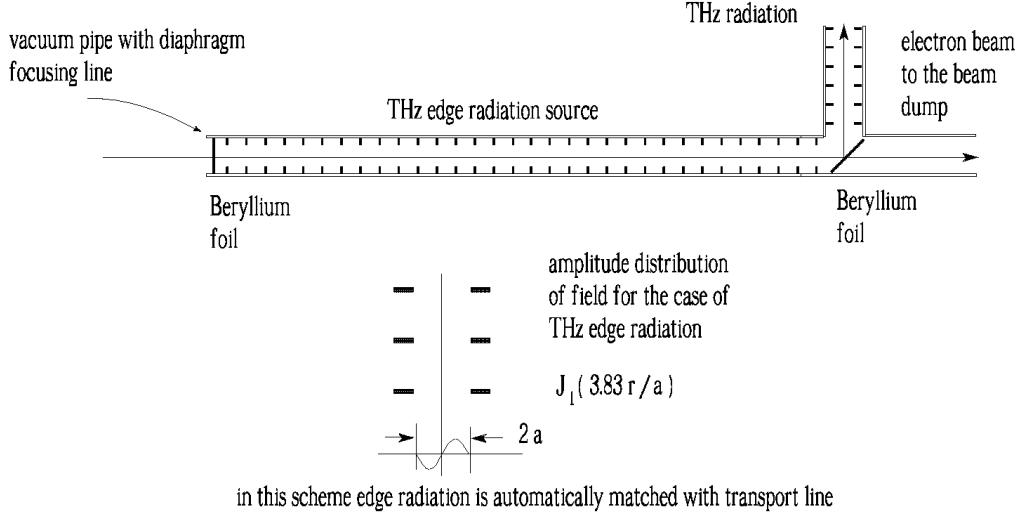


Fig. 2. Scheme for generating edge radiation in an iris line. In this scheme edge radiation is automatically matched to the transport line.

source is equipped with an iris line as well. We consider an electron beam moving along the z -axis inside the axisymmetric iris line, Fig. 2. Such source generates THz radiation with a fundamental mode that is automatically matched to that of the transmission line. We developed a theory of such kind of THz source using Vainstein impedance boundary conditions. As in the case of a microwave waveguide with resistive walls, one can use a Green's function approach to solve the field equations. Only non-azimuthal symmetric modes turn out to be driven by the uniform motion of the space charge distribution in an axisymmetric iris guide. From a physical viewpoint this is sound result. In fact, radiation is related with energy change of the particles, which happens through the scalar product of the electric field and velocity of the particles. Since the transverse velocity is equal to zero in the edge radiation case, symmetric modes cannot lead to any energy change of the electrons moving along the axis of the axisymmetric iris guide. Let us focus on the fundamental non symmetric mode only. Neglecting losses, for the moment, the amplitude for the orthogonal polarization components of the field in a cartesian coordinate system, where x and y are the transverse horizontal and vertical directions is given by:

$$\begin{aligned} A_x &= A_1 \cos(\phi) J_1(3.83r/a) \\ A_y &= A_1 \sin(\phi) J_1(3.83r/a), \end{aligned} \quad (1)$$

minimal size of the hole is defined by the condition that losses of the soft X-ray radiation from the baseline undulator due to the aperture limitation should be avoided. In any case, a hole with a diameter of a few mm will not perturb the soft X-ray beam nor the electron beam, nor the THz beam.

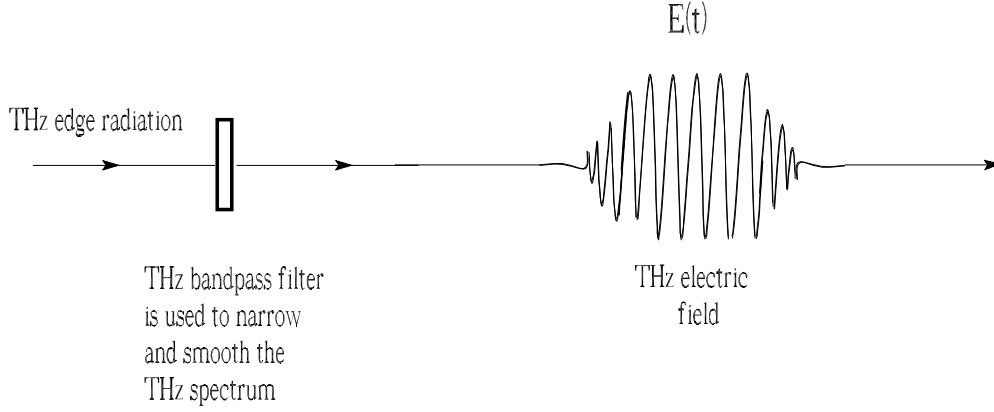


Fig. 3. For some experiments a smooth THz field is essential. In these cases, a THz bandpass filter should be used.

where J_1 indicates the first order Bessel function of the first kind, a is the iris radius, A_1 is a constant for a certain longitudinal position, and $r = \sqrt{x^2 + y^2}$, $\phi = \arctan(y/x)$ designate polar coordinates. It follows from Eq. (1) that the direction of the electric field is radial i.e. varies as a function of the transverse position. Therefore, for the edge radiation case we have two separate amplitudes for two orthogonal polarization directions. They are not azimuthal symmetric because they depend, respectively, on x/r and y/r , i.e. on the cosine and on the sine of the azimuthal angle. Only if one sums up the intensity patterns referring to the two polarization components one obtains the azimuthal symmetric intensity distribution

$$I = A_1^2 J_1^2(3.83r/a) . \quad (2)$$

Edge radiation is characterized by broad spectrum and radial polarization. Many practical applications require the control of the bandwidth and of the polarization of the THz pulse. The formation of a THz edge radiation pulse usually involves monochromatization and polarization filtering by inserting a THz band pass filter for reducing the spectral bandwidth and a wire grid polarizer for producing linearly polarized THz radiation, Fig. 3.

When dealing with a setup where THz radiation from an ultra relativistic electron beam is extracted by a mirror (in our case, the Be foil) and sent to a THz diagnostic station or user hutch, one usually talks about Backward Transition Radiation (BTR). The main problem to solve is in the specification of the electric field distribution at some position where the mirror is present.

It should be stressed that specification of the field at the mirror position must be considered as the first step to the specification of the field at the sample position. Such first step is considered separately, because the field at the mirror position is independent of the type of mirror and outcoupling optics. Once the field at the mirror position is known, the problem of specification of the field at the sample position can be solved with the help of Physical Optics techniques.

Let us discuss the problem of field characterization at the mirror position in more detail. When electrons are in unbounded space and come from an infinitely long straight line, the field distribution in the mirror plane can be calculated analytically following Ginzburg and Frank [21]. In most practical cases, however, the Ginzburg-Frank equation is not applicable because two basic assumptions of the analytical derivation are not fulfilled: the electron beam is moving inside the metallic vacuum chamber, which acts effectively like an overmoded waveguide, and the straight line has a finite length with a bending magnet at the upstream end. It is known (see e.g. [20]) that the Ginzburg-Frank theory is the limiting case of the more general theory of Edge Radiation (ER) in unbounded space. Emission of edge radiation in the presence of metallic boundaries has been a much less-treated subject in literature, compared to the unbounded space case. To the best of our knowledge, there is only one article reporting on edge radiation from electrons in a homogeneous metallic overmoded waveguide, in particular with circular cross-section [20]. The method described in [20] is therefore capable of treating realistic experimental setup. Here we apply method [20] to the case of an iris guide.

To fix ideas we focus our attention on the setup in Fig. 2. Electrons travel through the usual edge radiation setup, similarly as in [20]. The difference is that now we account for the presence of an iris guide along the straight section. Since electrons pass through an upstream edge screen, one may assume that the iris guide starts at the upstream screen position. In Section 5 we will calculate the field distribution at the mirror position, which should be subsequently propagated to the experimental hall. The presence of an upstream edge screen seems at first glance not necessary, because electrons come in any case from the straight section. However, due to variation of vacuum chamber cross-section upstream and downstream of the baseline undulator, and presence of the undulator magnetic field, characterization of the field distribution at the upstream open end of the iris guide is problematic. In spite of this, the electric field of the electron beam in the plane immediately behind the upstream screen can be well defined as zero, leading to extra simplifications. In this case we deal with a well defined problem and this allows us to characterize the field distribution at the end of the iris guide in the mirror plane.

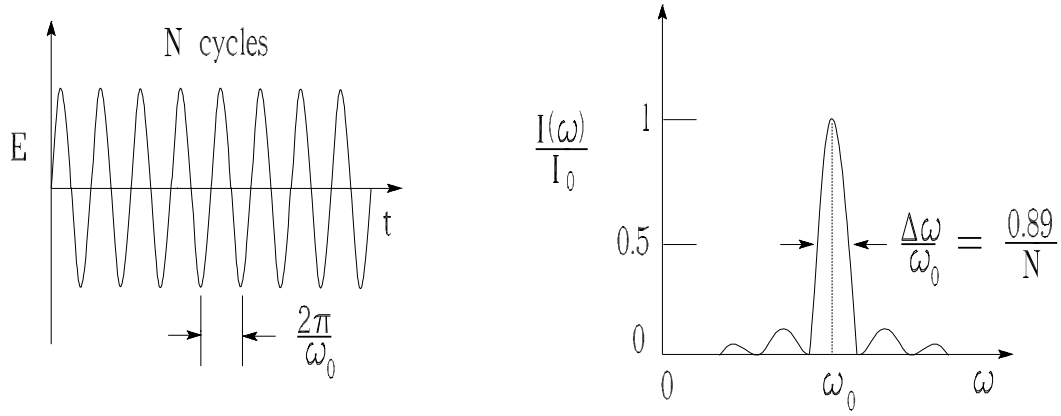


Fig. 4. Spectral properties of undulator radiation. A single electron passing an undulator radiates an electromagnetic wave with N_w cycles. For on-axis radiation the relative spectral FWHM bandwidth is $0.89/N_w$ near the central frequency.

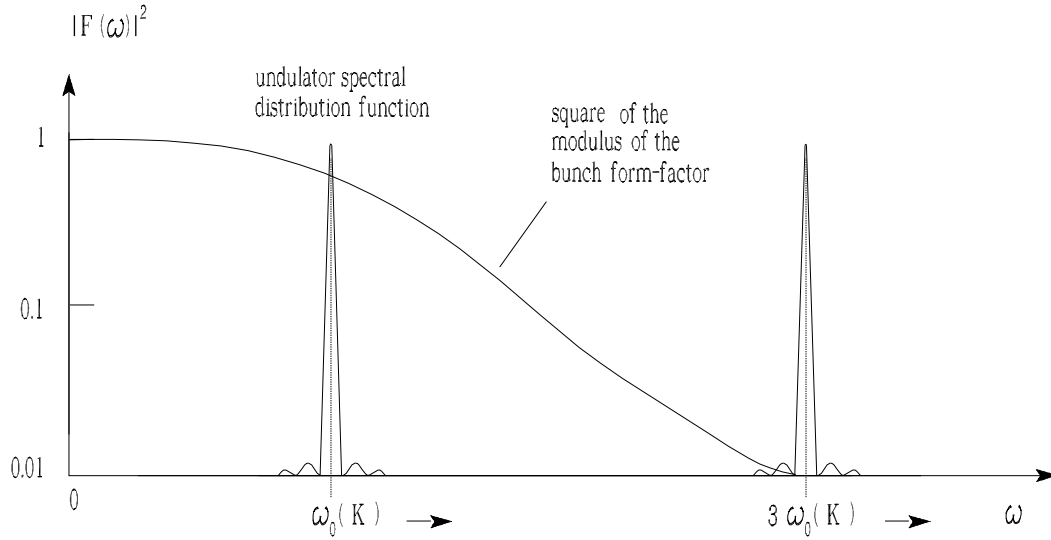


Fig. 5. Some typical spectra of the longitudinal electron distribution and undulator spectral distribution function. In general, the bunch form factor varies much more slowly in ω than the sharp undulator resonance term, and we can replace the form factor function by the constant value at the center of the sharp resonance curve.

2.2 Possible extension plans towards a coherent THz undulator source

The THz edge radiation source is limited as concerns the maximal field strength achievable. The optimal expansion strategy for the LCLS THz

source should include a THz undulator source to be installed at the LCLS baseline.

At resonance, undulator radiation can be described by three parameters: period λ_w , undulator parameter K , and number of periods, N_w . A single electron passing an undulator radiates an electromagnetic wave with N_w cycles, Fig. 4. For the radiation within the cone of half angle

$$\theta_c = \frac{\sqrt{1 + K^2/2}}{\gamma N_w} , \quad (3)$$

the relative spectral FWHM bandwidth is $\Delta\omega/\omega = 0.89/N_w$ near the central frequency

$$\omega_0 = 4\pi c \frac{\gamma^2}{\lambda_w(1 + K^2/2)} , \quad (4)$$

where γ is relativistic factor, Fig. 4. The proposed THz undulator is an inexpensive, planar electromagnetic device with ten periods, each 1.5 m long. At the operation wavelength of the THz source around 0.1 mm, the peak value of the magnetic field is about 1 T at an electron beam energy around 5 GeV.

In the case of the THz undulator at the LCLS, the electron beam transverse size is much smaller than the diffraction size. This means that, as pertains the characterization of the THz pulses, the electron beam can be modeled as a filament beam. In this case the electron beam current is made up of moving electrons randomly arriving at the entrance of the undulator

$$I(t) = (-e) \sum_{k=1}^{N_e} \delta(t - t_k) , \quad (5)$$

where $\delta(\cdot)$ is the Dirac delta function, $(-e)$ is the electron charge, N_e is number of electrons in a bunch, and t_k is the random arrival time of the electrons at the undulator entrance. The electron bunch profile is described by the profile function $F(t)$. $F(t)dt$ represents the probability of finding an electron between time t and time $t + dt$. The beam current averaged over an ensemble of bunches can then be written in the form:

$$\langle I(t) \rangle = (-e)N_e F(t) . \quad (6)$$

The radiation power at frequency ω , averaged over an ensemble, is given by the expression:

$$\langle P(\omega) \rangle = p(\omega)[N_e + N_e(N_e - 1)|\bar{F}(\omega)|^2], \quad (7)$$

where $p(\omega)$ is the radiation power from one electron and $\bar{F}(\omega)$ is the Fourier transform of the bunch profile function⁵. For wavelengths shorter than the bunch length the form factor reduces to zero. For wavelengths longer than the bunch length it approaches unity. A sample of undulator radiation spectrum is shown in Fig. 5. The distribution of the radiation energy within different harmonics depends on the value of the undulator parameter K . In our case of interest $K \gg 1$. Strong undulator maxima are present at $\omega = 3\omega_0$, $\omega = 5\omega_0$ and so forth. The energy measured by the detector is proportional to the convolution of the square modulus of the bunch form factor and of the spectral line of the undulator spectrum, as is illustrated in Fig. 5. Note that the bunch form factor behaves like an exponential function at high frequencies, and falls off rapidly for wavelengths shorter than the effective bunch length. For wavelength about three times shorter than the effective bunch length, the radiation power is reduced to about one percent of the maximum pulse energy at the fundamental harmonic. As a consequence, sharp changes of the bunch form factor result in attenuation of the higher undulator harmonics. In general, $|\bar{F}(\omega)|^2$ varies much slower in frequency than the sharp resonance term, and we can replace $|\bar{F}(\omega)|^2$ by the constant value $|\bar{F}(\omega_0)|^2$ at the center of the sharp resonance curve.

Let us consider the practically important case of an electron bunch with strongly non-Gaussian shape similar to that used to drive the LCLS. Fig. 6 shows the current distribution along the bunch [22]. The nominal charge is 0.25 nC. The electron bunch has a complicated shape, which is reflected in the squared modulus of the form factor shown in Fig. 7. In the case of the LCLS, the squared of the bunch form factor modulus falls off rapidly for wavelengths shorter than 0.06 mm. At the opposite extreme, the dependence of the form factor on the exact shape of the electron bunch is rather weak and can be ignored for wavelengths longer than 0.1 mm.

Similarly as for the edge radiation case, in order to solve the matching problem with the transmission line, we propose to generate the coherent THz undulator radiation directly in the iris line, Fig. 8.

Summing up, in view of the practical application to the THz undulator line at LCLS, there is a need to develop a comprehensive theory of undulator radiation in the presence of an iris line. As for the edge radiation source case, one can use a Green's function approach to solve the field equations, and the paraxial (overmoded waveguide) approximation can be used. In

⁵ A similar expression holds for the case of edge radiation. In fact, the electron beam transverse size is much smaller than the THz edge radiation diffraction size. This means that, as pertains the characterization of the THz edge radiation pulse, the electron beam can be modeled as a filament beam.

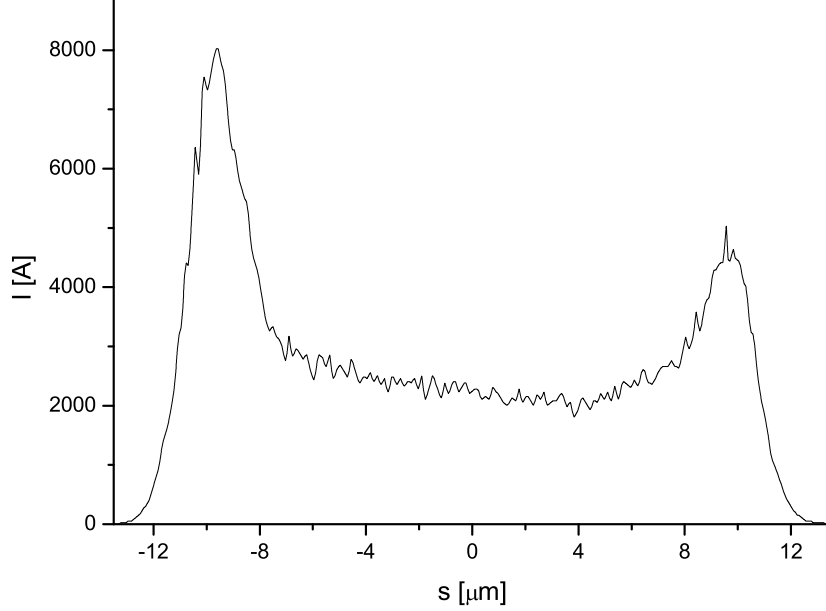


Fig. 6. Electron beam current profile at the LCLS, after [22].

addition to the paraxial approximation, in the undulator radiation case, the resonance approximation can be exploited too. We thus consider a large number of undulator periods and a frequency range of interest close to the fundamental harmonic. In free-space and under resonance approximation the radiation from a planar undulator is horizontally polarized, and thus constitutes a replica of the undulator polarization properties. Moreover, the field exhibits azimuthal symmetry. These properties are unvaried when an axisymmetric iris line is introduced. The wiggling amplitude of the electron in the undulator is taken to be small with respect to the dimension of the waveguide. This greatly simplifies analytical calculations, and describes our practical case of interest.

Applying the Green's function approach in this case one obtains a space invariant polarization and an azimuthal symmetric field distribution. In an axisymmetric iris guide only azimuthal symmetric modes turn out to be driven by the wiggling electron moving along the z axis. Let us focus on the first, dominant azimuthal symmetric mode. Neglecting losses, for the undulator radiation case we expect the following amplitude for the horizontally polarized radiation pulse:

$$A_x = A_0 J_0(2.4r/a) , \quad (8)$$

where J_0 is the Bessel function of the first kind of zero order, Fig. 8.

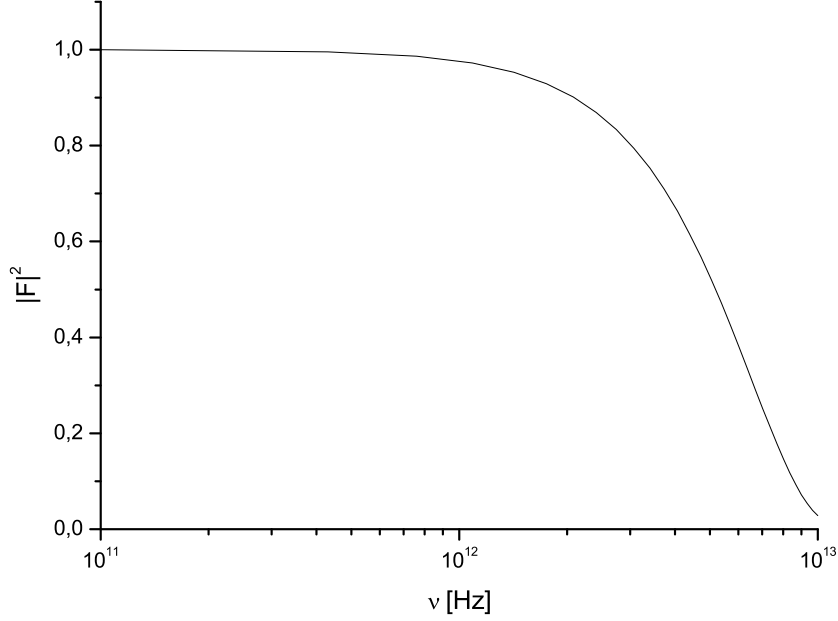


Fig. 7. Squared modulus of the electron beam form factor, $|\bar{F}|^2$, corresponding to the current profile in Fig. 6.

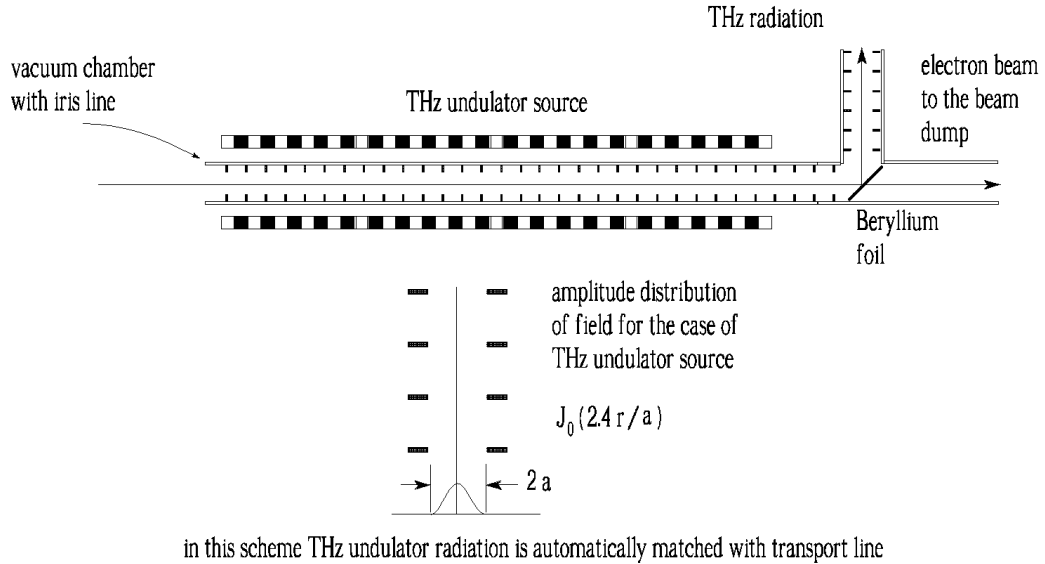


Fig. 8. Scheme for generating THz undulator radiation in an iris line. The THz undulator radiation is automatically matched to the iris transport line.

In contrast to edge radiation sources, THz undulator sources operate within the typical spectral window of undulator radiation $\Delta\omega/\omega \sim 1/N_w$ and the radiation is almost completely linearly polarized, Fig. 4. Additionally we

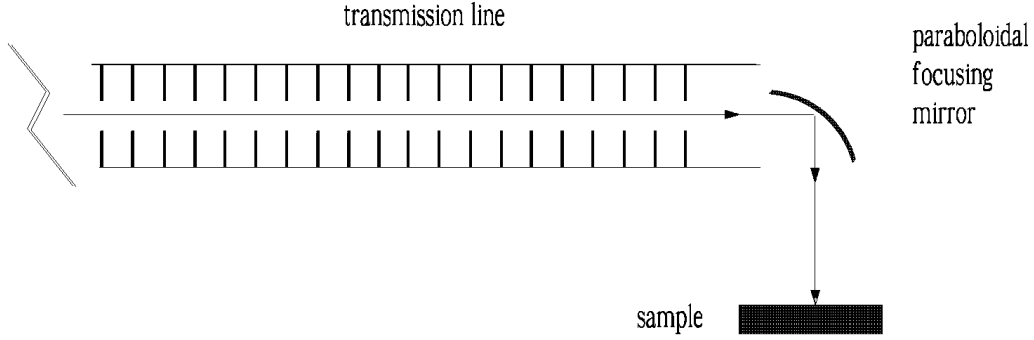


Fig. 9. A practical arrangement for the coherent THz source focusing system.

should consider the physics of the focusing process. In fact, at the end of the transmission line the THz pulses should be focused with the help of a converging lens or a paraboloidal focusing mirror, Fig. 9. The focusing spot of the first symmetric mode of an iris guide should be compared with the focusing spot of the first non symmetric mode of the same iris guide. Summing up, in view of practical applications, an important advantage of THz undulator sources over edge radiation sources is a few ten times (for $N_w \sim 10$) higher intensity on the sample as compared to THz edge radiation sources at the same electron beam parameters.

3 Theoretical background of an iris line

We begin our theoretical investigation from Fig. 10, a sketch of an iris line, which is formed by perfectly absorbing screens of infinite extent with collinear circular holes. The radius of the holes is indicated with a , while the distance between two screens is indicated with b .

An analysis of the behavior of an electromagnetic wave passing through the line was given first in terms of numerical calculations by Fox and Li [6], and then in terms of analytical results by Vainstein [7, 8].

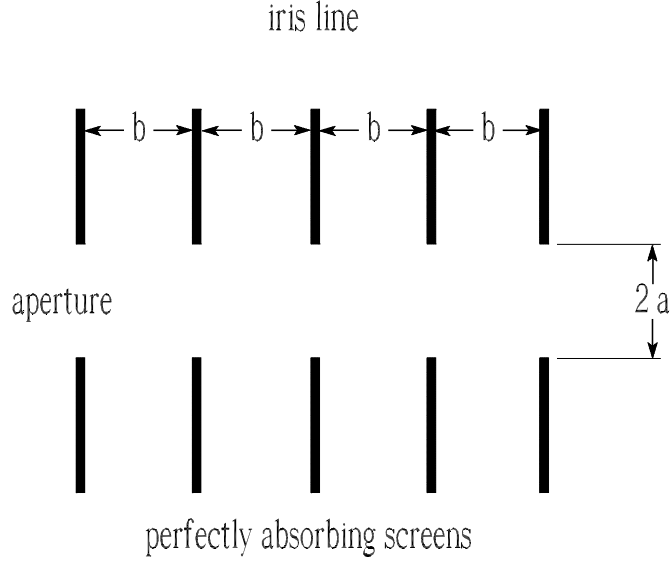


Fig. 10. Iris line comprising a series of collinear identical apertures cut into parallel and equally spaced black (i.e. perfectly absorbing) partitions of infinite extent.

3.1 Numerical method

Consider the iris guide in Fig. 10, and call $\widetilde{E}(\vec{r}', 0)$ the transverse profile of a given polarization component of the slowly varying envelope of the electric field on the iris at $z = 0$ in the space-frequency domain, that is at a given fixed frequency ω . The field at the iris at $z = b$ is easily obtained as

$$\widetilde{E}(\vec{r}, b) = \int d\vec{r}' K(\vec{r}, \vec{r}'; b) \widetilde{E}(\vec{r}', 0), \quad (9)$$

where function $K(\vec{r}, \vec{r}'; z)$ is a Green's function, or propagator, for the paraxial wave equation which describes the field evolution. In physical optics one uses the Fresnel propagator which is the solution of the wave equation for unbounded space (with zero boundary at infinity, outgoing wave). In the case of a circular shape of the iris one may use polar coordinates and obtain [6]:

$$\widetilde{E}(r, \phi, b) = \int_0^{2\pi} d\phi' \int_0^a dr' r' K(r, r', \phi, \phi'; b) \widetilde{E}(r', \phi', 0), \quad (10)$$

with

$$K(r, r', \phi, \phi'; b) = \frac{i\omega \exp[-ikb]}{cb} \exp \left[-ik \left(\frac{r^2 + r'^2}{2b} - \frac{rr'}{b} \cos(\phi - \phi') \right) \right], \quad (11)$$

which is valid at large Fresnel numbers $a^2/(b\lambda) \gg 1$. Iterations can be performed iris after iris, to obtain the field at the position of any iris at arbitrary distance from the entrance. The modes of the waveguide are, by definition, field distributions that do not depend on the longitudinal z coordinate. Since we are dealing with the modes of an empty waveguide with no gain medium, the mode amplitudes decreases along the z axis due to diffraction at the irises. However, the shape or spatial pattern of the field distribution defining a given mode does not. It follows that the field profile of a certain mode at the $n+1$ iris, $\tilde{E}(x, y, (n+1)b)$ is simply $\tilde{E}(x, y, nb)$ multiplied by some complex number⁶ γ . It follows that the following integral equation holds

$$\gamma \tilde{E}(\vec{r}) = \int d\vec{r}' K(\vec{r}, \vec{r}'; b) \tilde{E}(\vec{r}'), \quad (12)$$

where for simplicity we drop the explicit reference to the z dependence.

Note that Eq. (12) may be written in the operator form

$$\Gamma \tilde{E} = \gamma \tilde{E}, \quad (13)$$

where Γ is the operator corresponding to a trip between two successive irises:

$$\Gamma = \int d\vec{r}' K(\vec{r}, \vec{r}'; b). \quad (14)$$

According to Eq. (14), the modes of the iris guide are the eigenfunctions of the operator Γ for the guide. The number γ is, instead, the eigenvalue corresponding to the eigenfunction $\tilde{E}(\vec{r})$. In contrast with usual quantum-mechanical situations, where eigenvalue equations include Hermitian operator, here Γ is generally not Hermitian. For instance, its eigenvalues are complex, whereas the eigenvalues of a Hermitian operator are always real.

Due to diffractive losses at the irises, the total energy associated with the field inside the guide diminishes, and one must have $|\gamma| < 1$. The iris guide modes may be found by solving Eq. (9) numerically. This is usually done according to the method developed by Fox and Li in 1961. One starts by assuming some initial field $\tilde{E}(x, y, 0)$ on an iris, usually just $\tilde{E}(x, y, 0) = \text{constant}$. The field is then propagated to the other iris by calculating the integral in

⁶ Not to be confused with the relativistic factor γ of the electrons.

Eq. (9) numerically and iterating until the field on the irises is unchanged (within some prescribed numerical error) on successive iterations, except for a constant factor γ . The field yielded by this method is a solution of Eq. (12), that is, it is a mode of iris guide. Only one mode, that is the one with smaller losses per iteration will be returned following this procedure. However, higher-loss modes can also be obtained. For example, looking for solutions with the form

$$\widetilde{E}(r, \phi, z) = R_n(r, z) \exp(-in\phi), \quad (15)$$

with $n = 0, 1, 2, \dots$, Eq. (10) and Eq. (11) can be rewritten for $R_n(r, z)$ after integrating in $d\phi'$ as

$$R_n(r, b) = \int_0^a dr' r' K_r(r, r'; b) R_n(r', 0), \quad (16)$$

with

$$K_r(r, r'; b) = \frac{i^{n+1} \omega}{cb} J_n \left(\frac{krr'}{b} \right) \exp \left[-ik \frac{r^2 + r'^2}{2b} \right], \quad (17)$$

which allows to find different modes as n varies.

3.2 Analytical method

The analytical method by Vainstein is based on the introduction of particular, complex boundary conditions, which are called impedance boundary conditions. Once these boundary conditions for the field are formulated on the virtual side surface of the iris line, the original problem, which is about an open waveguide excitation, is simplified to that of a closed waveguide.

In order to understand how the impedance boundary conditions come into play, we consider, following [7, 8], the simpler case of diffraction of a plane wave at a stack of semi-infinite screens, as depicted in Fig. 11. We assume here that the screens are totally absorbing. When the wave illuminates one screen, the total field can be presented as the sum of the unperturbed wave and a cylindrical wave generated by an image source at the edge of the screen. The unperturbed wave propagates up to the following screen and produces another cylindrical wave at the second edge. As a result, the diffracted wave is given by the sum of many cylindrical waves generated

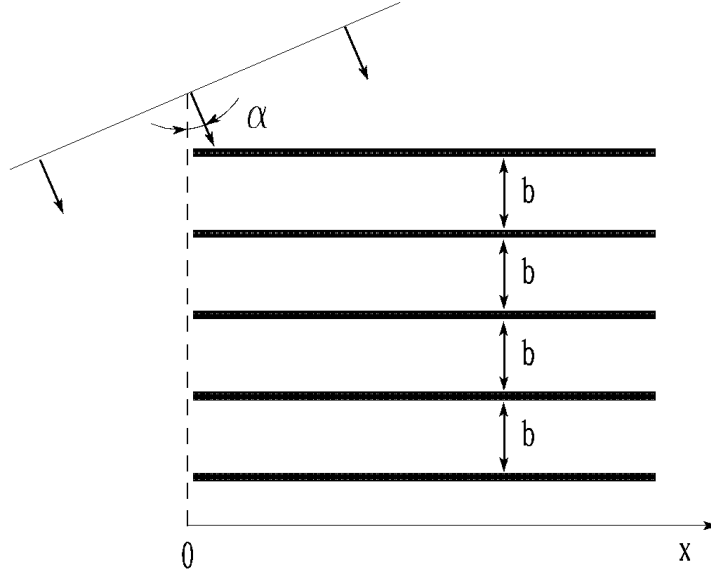


Fig. 11. Diffraction of plane wave at semi-infinite screens.

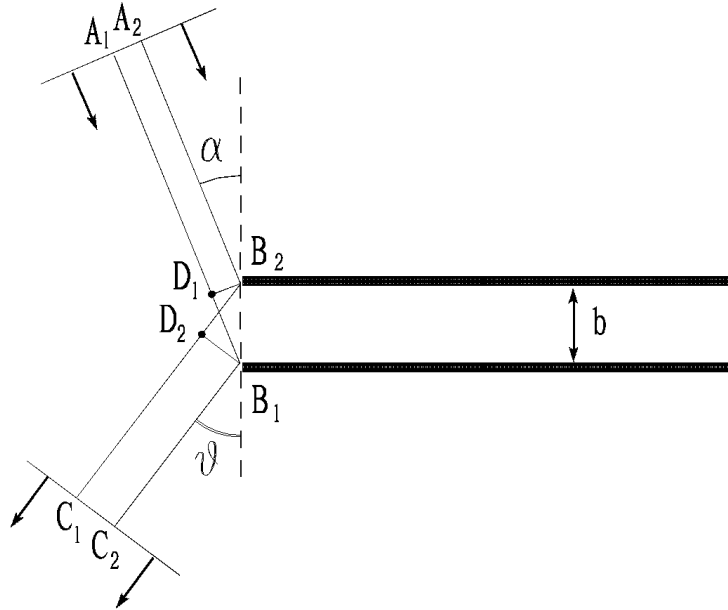


Fig. 12. Geometry of the diffracted wave.

at the edges of the screens. Constructive interference takes place only along a series of privileged directions. This is shown in Fig. 12. The reader can easily recognize that the path difference between $A_1B_1C_1$ and $A_2B_2C_2$ is just given by $D_1B_1 - D_2B_2 \simeq b(\theta^2 - \alpha^2)/2$. Constructive interference is given for

$$kb(\theta^2 - \alpha^2)/2 \simeq 2\pi n \quad (18)$$

with $n = 0, 1, 2, \dots$, while it is zero at all other directions. For $n = 0$ one

obtains the zeroth order diffracted wave, which is just "reflected". When the angle of incidence is small $\alpha^2 \ll \lambda/(2\pi b)$, the screen does not absorb, but rather reflect the wave. The finding of the reflection coefficient pertaining the zeroth order diffraction is due to Vainstein, and reads

$$R_0 = -\exp\left[-\beta_0(1-i)\alpha(kb)^{1/2}\right], \quad (19)$$

with⁷ $\beta_0 = 0.824$. Note that R_0 is complex, meaning that the zeroth order diffracted wave suffers phase shift and attenuation. The impedance boundary condition are a consequence of Eq. (19).

In fact, the slowly varying envelope of the total field in the plane of the screen turns out to be written as

$$\widetilde{E}(x) = A[\exp(ik_x x) + R_0 \exp(-ik_x x)], \quad (20)$$

where A is just the amplitude of the incident field. Then, using $\alpha \simeq k_x/k_z$ and $k_x^2 + k_z^2 = 4\pi^2/\lambda$, and taking advantage of Eq. (19) one obtains that the logarithmic derivative of \widetilde{E} at the edge of the screen can be written as

$$\frac{d \ln(\widetilde{E})}{dx} \Big|_{x=0} = \frac{1}{\widetilde{E}} \frac{d\widetilde{E}}{dx} \Big|_{x=0} = ik_x \frac{1-R_0}{1+R_0}. \quad (21)$$

Assuming $\alpha \sqrt{kb} \ll 1$ and using the expansion $\exp[-\beta_0(1-i)\alpha \sqrt{kb}] \simeq 1 - \beta_0(1-i)\alpha \sqrt{kb}$, we obtain

$$\frac{d \ln(\widetilde{E})}{dx} \Big|_{x=0} = \frac{1}{\widetilde{E}} \frac{d\widetilde{E}}{dx} \Big|_{x=0} = -\left[\beta_0(1+i) \sqrt{\lambda b/(8\pi)}\right]^{-1}. \quad (22)$$

The main feature of this formula is that the term k_x is completely excluded from it, which allows one to use Eq. (22) as an approximate boundary condition. Note that this is valid not only for plane waves. In fact, any wave can be decomposed in terms of a linear superposition of plane waves. Since Eq. (22) is valid for each component, it must be valid for their linear superposition as well. Eq. (22) can also be extended for any shape of the (virtual) boundary surface, provided that the typical value of the curvature radius is much larger than the wavelength. Eq. (22) is named after Vainstein, who first derived it, and can be written in vector form as

⁷ β_0 turns out to be related with one of the most famous mathematical functions, the Riemann zeta function ζ . In fact, it is given by $-\zeta(1/2)/\sqrt{\pi}$, see [7, 8].

$$\left[\vec{E} + (1+i)\beta_0 \sqrt{cb/(4\omega)} (\vec{n} \cdot \vec{\nabla}_\perp) \vec{E} \right]_S = 0, \quad (23)$$

where S is the cylindrical virtual surface of the iris guide, and \vec{n} is the unit vector normal to S . Let us consider axially symmetric iris line. We seek a solution for the field amplitude $\vec{E}(r, \phi, z)$ in the form

$$\vec{E} = u_{nj}(r) \exp[-in\phi - ik_z z], \quad (24)$$

with $n = 0, 1, 2, \dots$. The functions $u_{nk}(r)$ are subjected to the following homogeneous equations

$$r^2 u_{nj}'' + r u_{nj}' + [(k_{nj})^2 - n^2] u_{nj} = 0, \quad (25)$$

and satisfy the boundary conditions

$$[u_{nj} + (1+i)\beta_0 \sqrt{cb/(4\omega)} u_{nj}']_{r=a} = 0. \quad (26)$$

In the first order of the small parameter $M = (8\pi N)^{-1/2}$, where $N = a^2/\lambda b$ is the Fresnel number with a the iris radius, the functions u_{nj} assume the form

$$u_{nj} = J_n(k_{nj}r) \quad (27)$$

where

$$k_{nj} = \frac{v_{nj}}{a} [1 - (1+i)\beta_0 M], \quad (28)$$

and v_{nj} is the j -th root of the n -th order Bessel function of the first kind (i.e. $J_n(v_{nj}) = 0$). Substituting the expression for k_{nj} into the dispersion relation

$$k_z^2 + k_{nj}^2 = \frac{\omega^2}{c^2} \quad (29)$$

we obtain the following expression for k_z :

$$k_z b = \frac{\omega b}{c} - 2v_{nj}^2 M^2 + 4v_{nj}^2 M^3 (1+i)\beta_0. \quad (30)$$

For the eigenmode with transverse wavenumber k_{nj} , the fraction of the radiation power losses per transit of one iris is given by

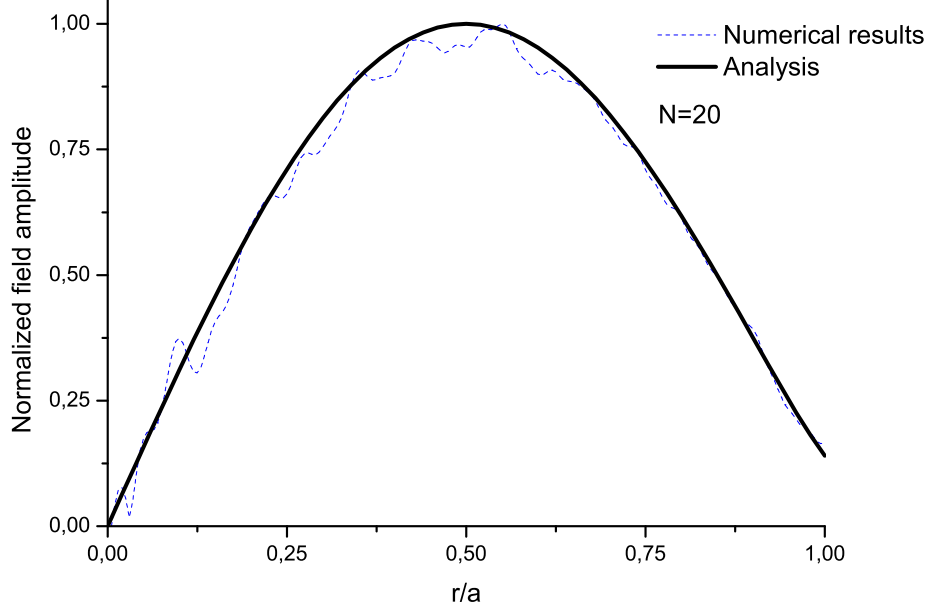


Fig. 13. Comparison of the fundamental non-symmetric mode derived analytically and numerically for the Fresnel number $N = a^2/(\lambda b) = 20$.

$$2\text{Im}(k_z b) = 8v_{nj}^2 M^3 \beta_0. \quad (31)$$

The relative loss of the j -th mode of order n after traveling for a distance z is therefore given by

$$\left(\frac{\Delta W}{W}\right)_{nj} = 1 - \exp\left(-\frac{v_{nj}^2 \beta_0}{(2\pi N)^{3/2}} \frac{z}{b}\right) = 1 - \exp\left(-\frac{v_{nj}^2 \beta_0 (\lambda b)^{3/2}}{(2\pi)^{3/2} a^3} \frac{z}{b}\right). \quad (32)$$

Due to the exponential dependence on v_{nj}^2 , only the lower order modes tend to survive. Note that the exponent in Eq. (32) depends on the distance between two irises, b , only weakly as \sqrt{b} , while there is a much stronger dependence on λ and a .

3.3 Comparison between analytical and numerical methods

Comparisons between analytical and numerical results are given in Fig. 13 and Fig. 14, respectively for the edge radiation and undulator cases. For the sake of completeness, Fig. 15 shows a comparison between the phase of the main symmetric mode calculated analytically and numerically as well.

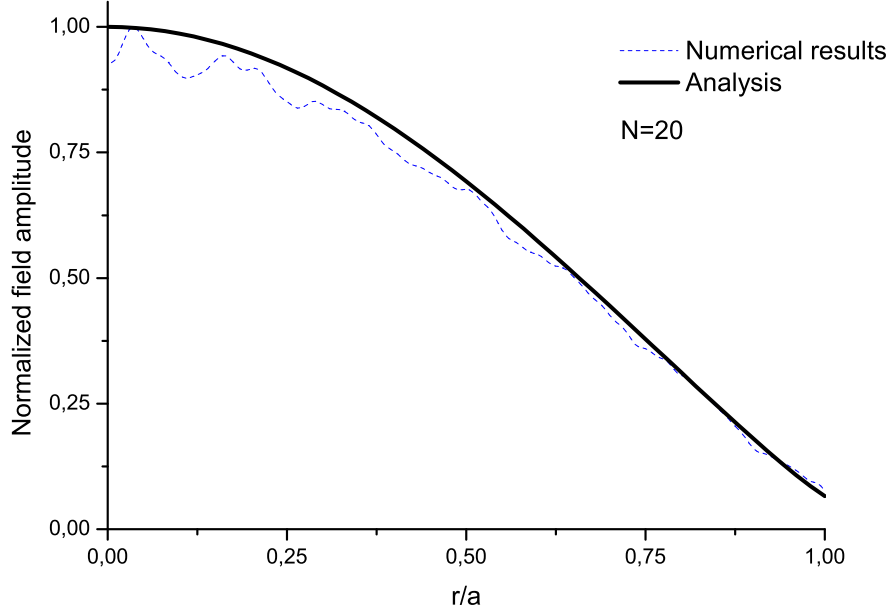


Fig. 14. Comparison of the fundamental symmetric mode derived analytically and numerically for the Fresnel number $N = a^2/(\lambda b) = 20$.

Note that there are some minor differences between analytical and numerical results. These differences, in form of ripples in the numerically calculated modes, are not a residual from higher order modes. In fact, they do not disappear as the number of iterations increases. They can be explained noting that Eq. (22) only accounts for the zeroth order diffraction, see Eq. (19) with $n = 0$, while the numerical method by Fox and Li accounts for all diffraction orders. As a result, some difference should be expected between the iris line modes calculated with the two methods.

A comparison between Eq. (32) and losses from numerical calculations is given in Fig. 16 as a function of the Fresnel number for $n = 0$, and in Fig. 17 for $n = 1$. The convergence of these results as a function of the iteration number is exemplified in Fig. 18 in the case $N = 20$. After a large number of iteration, the power losses between two successive irises becomes constant. This constant is the result finally plotted in Fig. 16 and Fig. 17.

3.4 Technical requirements

It is important to study the influence of imperfections in the construction of the iris line on its nominal properties. With little modification, the computer technique by Fox and Li can be used to study the effects of misalignment of

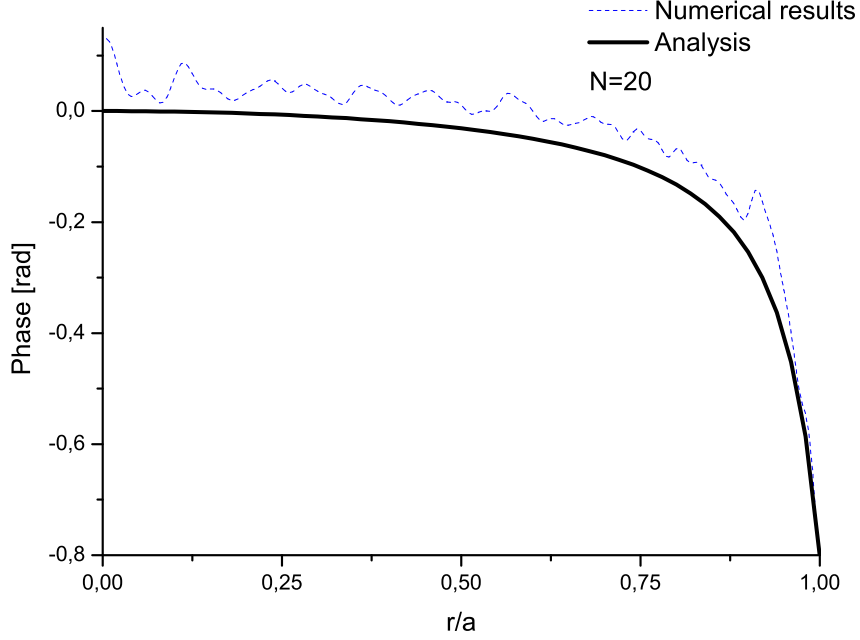


Fig. 15. Comparison of the phase of the fundamental symmetric mode derived analytically and numerically for the Fresnel number $N = a^2/(\lambda b) = 20$.

iris positions in the longitudinal direction. The importance of this effect is shown in Fig. 19 for $\lambda = 0.1$ mm, $b = 30$ cm, and $a = 1.35$ cm. When the irises are adjusted with an accuracy of 1 mm (rms) the irregularities of the iris line do not result (with graphical accuracy) in additional diffraction losses. The result that the iris line is a "non-resonant" device should not be surprising, and can be deduced from the explanations presented above in this Section.

Let us now study the requirements on the accuracy of the transverse alignment between the irises. When one of the iris is shifted off the axis, it may cause distortion in amplitude and phase of the diffracted wave. To estimate the change in amplitude, one should remember that the amplitude of the wave produced by the edge of the iris (see Fig. 11) in the region of the next iris is proportional to the Fresnel integral

$$F(\psi) = \int_{\psi}^{\infty} \exp(i\tau^2) d\tau , \quad (33)$$

where $\psi = x \sqrt{\pi/(\lambda b)}$. The Fresnel integral $F(\psi)$ is decreased by about a factor 2 when x changes from 0 to $\sqrt{\lambda b/\pi}$. Therefore, one can consider the region for $x > \sqrt{\lambda b/\pi}$ as the region of the shadow. If an iris is shifted off

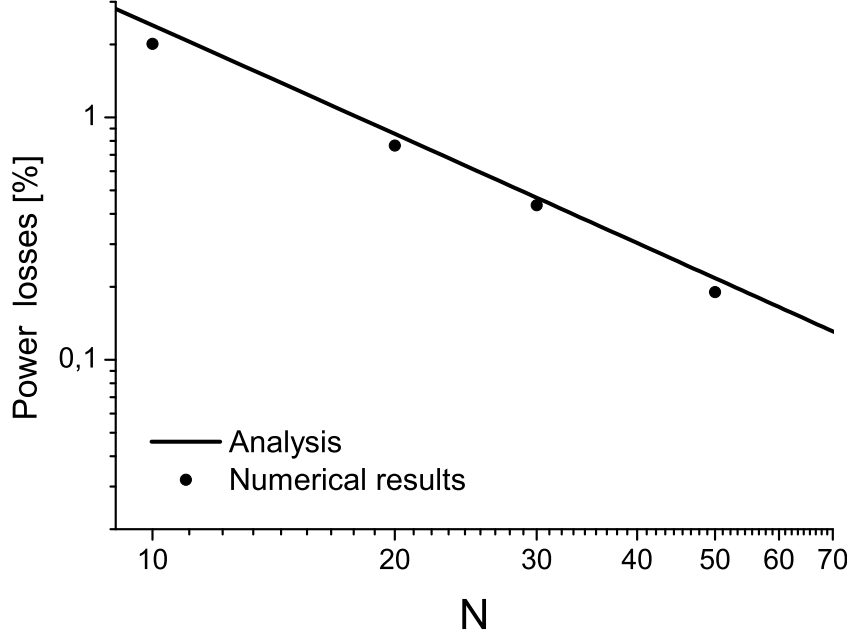


Fig. 16. Power losses per transit between two successive irises vs $N = a^2/(\lambda b)$ for the first non-symmetric mode. The curve is calculated with the analytical formula Eq. (32). Circles are the result of calculations with the Fox-Li iterative method.

the axis by a value $\sim \sqrt{\lambda b/\pi}$, either such iris or the next one fall into the region of the shadow and does not produce any diffracted wave. To estimate phase errors, we consider Fig. 12. One can see that a shift of the iris by a certain value δx in the transverse direction causes a phase shift of the mirror-reflected wave of about $2\alpha\omega \cdot \delta x/c$. A phase shift equal to π is achieved at $\delta x = \lambda/(4\alpha)$. In paraxial approximation $\alpha^2 \ll \lambda/(\pi b)$, and the value of the admissible shift of the iris is mainly defined by aperture restrictions, and not by phase distortions. Summing up, requirements on the accuracy of the transverse alignment of the irises is given by $\delta x \ll \sqrt{\lambda b/\pi}$. For $\lambda \simeq 0.1$ mm, $b \simeq 30$ cm, we estimate a restriction $\delta x \ll 3$ mm.

Finally, with little modifications, the computer technique employed up to now can be used to study the effects of particular aperture restrictions. When the radius of the irises are manufactured with an accuracy δa , these irregularities result in extra diffraction losses. The importance of this effect is shown in Fig. 20. Simulations show that when the irises are manufactured with an accuracy better than 1 mm in both transverse and longitudinal direction, manufacturing errors do not result in extra diffraction losses in our case of interest.

In conclusion it should be noticed that requirements on the transverse extent

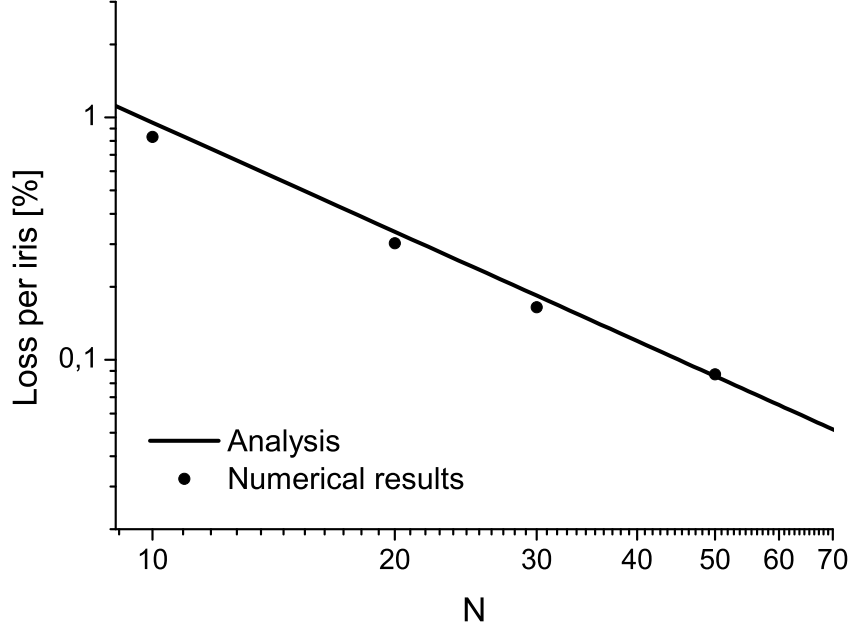


Fig. 17. Power losses per transit between two successive irises vs $N = a^2/(\lambda b)$ for the first symmetric mode. The curve is calculated with the analytical formula Eq. (32). Circles are the result of calculations with the Fox-Li iterative method.

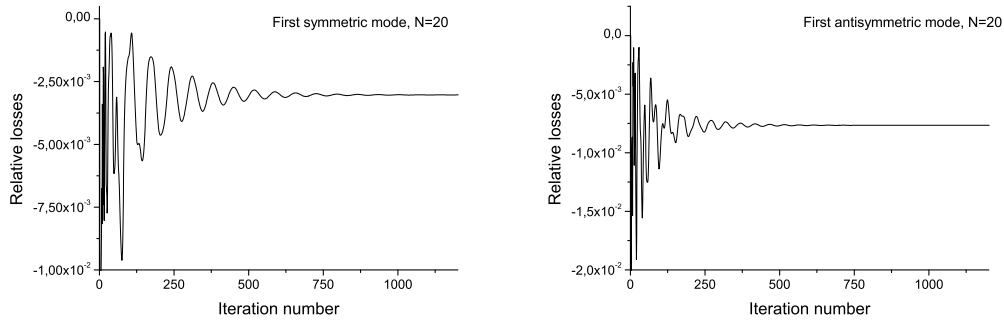


Fig. 18. Power losses between two successive irises at $N = 20$ as a function of the iteration number. Left plot: first symmetric mode. Right plot: first antisymmetric mode.

of the screens i.e on the difference between the pipe radius R and the hole radius a is given by $R - a \gg \sqrt{\lambda b/\pi} \approx 3 \text{ mm}$. Additionally, there is no need to use completely absorbing screens in the iris line. It would even be preferable to use reflecting screens. In fact, within the accepted limitations, reflecting screens are almost identical to absorbing screens as concerns diffraction effects.

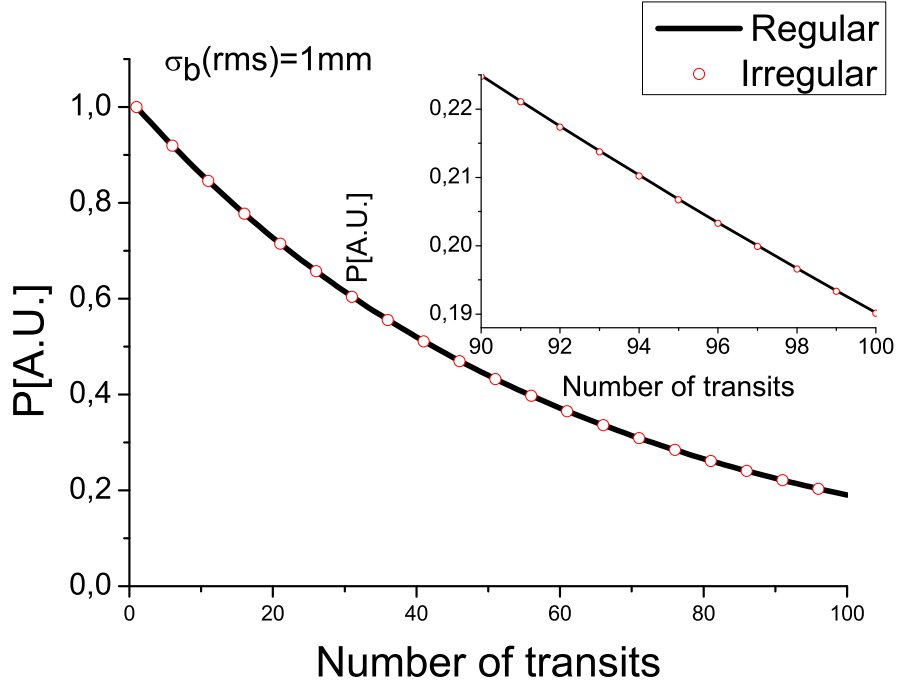


Fig. 19. Power of the principal symmetric mode versus number of transits. Calculations have been performed with the Fox and Li method. Here the wavelength $\lambda = 0.1$ mm, the iris separation is $b = 30$ cm, the hole radius is $a = 1.35$ cm. The solid curve corresponds to the perfect iris line. The circles represent results from numerical simulations when distances between irises are randomly distributed around $b = 30$ cm with rms $\sigma_b = 1$ mm. The inset is an enlargement of a region of the main plot.

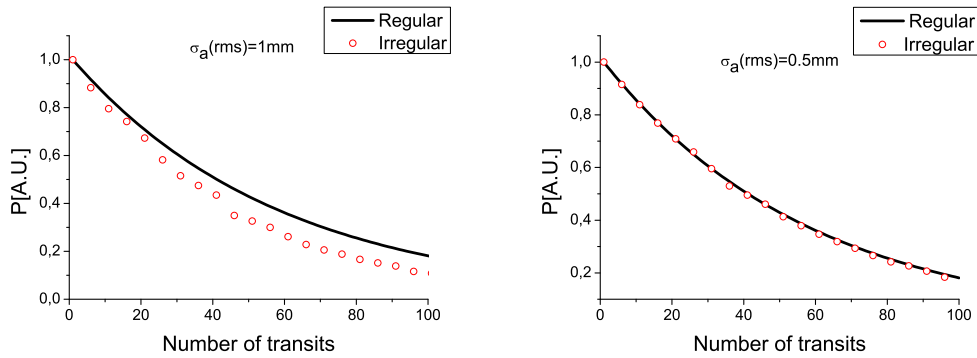


Fig. 20. Simulated power losses due to aperture distortions as a function of the number of transits. The radius of irises are randomly distributed with an rms value of 1 mm (left plot) and 0.5 mm (right plot). Here the average hole radius is $a = 1.35$ cm, $b = 30$ cm, $\lambda = 0.1$ mm.

3.5 Focusing of fundamental edge radiation and undulator radiation modes

For practical experimental purposes, edge or undulator THz radiation needs to be focused onto the sample. This can be done by placing a focusing mirror

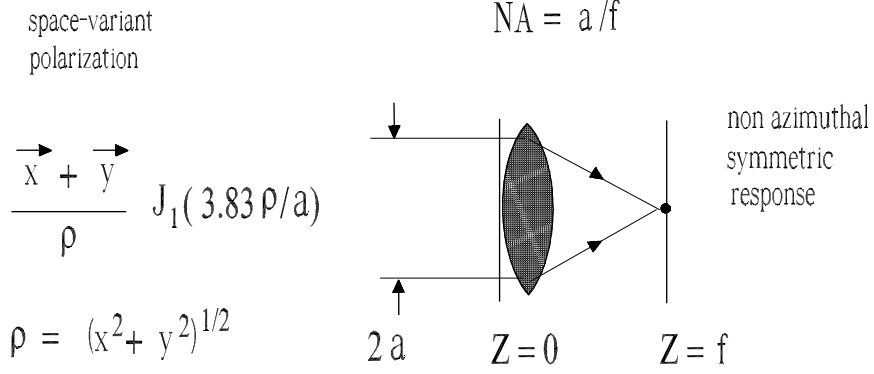


Fig. 21. Single lens focusing system for the edge radiation source.

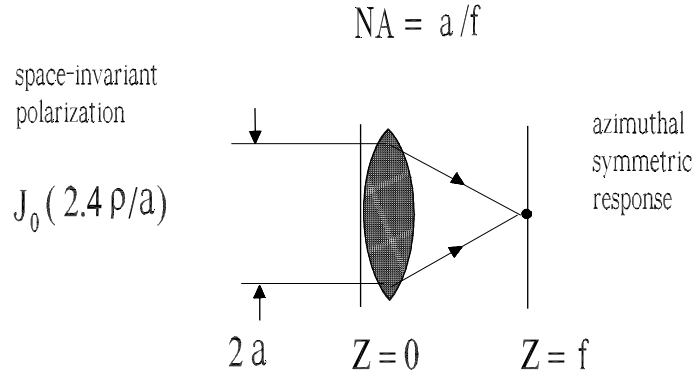


Fig. 22. Single lens focusing system for the undulator radiation source.

at the exit of the iris guide, and by positioning the sample in the focus. We will treat the mirror as a thin lens with focal length f . The focusing system for the edge radiation and for the undulator radiation sources are illustrated in Fig. 21 and Fig. 22 respectively.

In general, in the space-frequency domain, the relation between the slowly varying envelope of the field $\vec{E}(0, \vec{r})$ at the position immediately in front of the lens, $z_{\text{lens}} = 0$, and the slowly varying envelope of the field $\vec{E}(f, \vec{r}_f)$ at the

sample position $z_{\text{sample}} = f$, is given by

$$\vec{\vec{E}}(f, \vec{r}_f) = \frac{i\omega}{2\pi cf} \exp\left[\frac{i\omega r_f^2}{2cf}\right] \int d\vec{r'} \vec{\vec{E}}(0, \vec{r'}) P(\vec{r'}) \exp\left[-\frac{i\omega \vec{r}_f \cdot \vec{r'}}{cf}\right], \quad (34)$$

where $P(\vec{r'})$ indicates the pupil function, and will be assumed here to be

$$P(\vec{r'}) = 1 \text{ for } r < a, \text{ } P(\vec{r'}) = 0 \text{ otherwise.} \quad (35)$$

Differences between the edge radiation and the undulator radiation case arise due to the different expressions for $\vec{\vec{E}}(0, \vec{r'})$. In particular, the radial polarization of the edge radiation pulse leads to a non-azimuthal symmetric response, whereas the linear polarization of the undulator radiation pulse yields an azimuthal symmetric response.

From Eq. (1) we know that in the edge radiation case

$$\vec{\vec{E}}(0, \vec{r'}) = A_1 J_1\left(\frac{v_{11} r'}{a}\right) [\cos(\phi') \vec{e}_x + \sin(\phi') \vec{e}_y], \quad (36)$$

while from Eq. (8) we know that in the undulator case the field at the position immediately in front of the lens is

$$\vec{\vec{E}}(0, \vec{r'}) = A_0 J_0\left(\frac{v_{01} r'}{a}\right) \vec{e}_x. \quad (37)$$

Substitution of, respectively, Eq. (36) and Eq. (37) in Eq. (34) yields the following results for the field at the sample in the case of an edge radiation pulse

$$\vec{\vec{E}}(f, \vec{r}_f) = \frac{\omega A_1}{cf a^2} \left(v_{11}^2 - \frac{r_f^2 \omega^2 a^2}{c^2 f^2}\right)^{-1} v_{11} J_0(v_{11}) \exp\left[\frac{i\omega r_f^2}{2cf}\right] J_1\left(\frac{\omega a}{cf} r_f\right), \quad (38)$$

and of an undulator pulse

$$\vec{\vec{E}}(f, \vec{r}_f) = \frac{i\omega A_0}{cf a^2} \left(v_{01}^2 - \frac{r_f^2 \omega^2 a^2}{c^2 f^2}\right)^{-1} v_{01} J_1(v_{01}) \exp\left[\frac{i\omega r_f^2}{2cf}\right] J_0\left(\frac{\omega a}{cf} r_f\right). \quad (39)$$

It is possible to give a quantitative measure of how well one can focus edge radiation pulses compared to undulator pulses. This measure is simply

given by the ratio between the maximum of intensity in the two cases, assuming that the energy per mode per unit spectral interval is the same.

First note that the energy per unit spectral interval per unit surface after focusing is proportional to the squared modulus of Eq. (38) and Eq. (39), respectively for the edge radiation and for the undulator case. The assumption of same energy per mode per unit spectral interval can be enforced by means of the following relation between the field amplitudes:

$$\left(\frac{A_1}{A_0}\right)^2 = \frac{J_1^2(\nu_{01})}{J_0^2(\nu_{11})}, \quad (40)$$

where A_0 and A_1 enter in the expression for the field as in Eq. (39) and Eq. (38). The energy per unit spectral interval per unit surface is given by

$$\frac{dW}{d\omega dS} = \frac{c}{4\pi^2} \left| \vec{E} \right|^2. \quad (41)$$

Note that the transverse dependence of Eq. (38) and Eq. (39) is in the normalized distance $\hat{r}_f = r_f \omega a / (cf)$. For the non-symmetric mode case, the maximum of energy density in the focal plane occurs at $\hat{r}_f \simeq 2.84$. For the symmetric mode case, such maximum occurs at $\hat{r}_f = 0$. The relative efficiency with which the non-symmetric mode can be focused compared with the symmetric mode is given by $\eta \sim 1$. The outcome of this calculation is different from what one would have intuitively guessed. If we assume the same energy in symmetric and non-symmetric modes, after focusing we obtain practically the same maximum energy density on the sample. Our consideration is only valid for the aberration-free lens case and within a paraxial treatment i.e. for numerical aperture of the lens $NA = a/f < 0.3$. In fact, the field distribution of the non-symmetric mode, Eq. (36) is quite different compared to the symmetric mode distribution Eq. (37), and the aberrations can have a significant effect on the relative mode efficiency η .

4 Green's function for an axisymmetric iris line

Let us consider the motion of an ultrarelativistic electron in an axisymmetric iris line, and indicate with $\vec{E}(\vec{r}, z, \omega)$ the Fourier transform of the transverse electric field generated by the electron. Since the radiation formation length is much longer than the reduced wavelength $\lambda = c/\omega$, the electric field envelope $\vec{E} = \vec{E} \exp[-i\omega z/c]$ turns out to be a slowly varying function of z with

respect to the wavelength, and it obeys the paraxial Maxwell equation⁸:

$$\vec{\mathcal{D}}\vec{E}(z, \vec{r}) = \vec{g}(z, \vec{r}) \quad (42)$$

The differential operator \mathcal{D} in Eq. (42) is defined by

$$\mathcal{D} \equiv \left(\nabla_{\perp}^2 + \frac{2i\omega}{c} \frac{\partial}{\partial z} \right), \quad (43)$$

where ∇_{\perp}^2 is the Laplacian operator over transverse cartesian coordinates. The vector $\vec{g}(z, \vec{r})$ is specified by the trajectory of the source electron, $\vec{r}'(z)$, and is written as

$$\vec{g} = \frac{4\pi e}{c} \exp \left[i \int_0^z d\bar{z} \frac{\omega}{2\gamma_z^2(\bar{z})c} \right] \left[\frac{i\omega}{c^2} \vec{v}(z) - \vec{\nabla}_{\perp} \right] \delta(\vec{r} - \vec{r}'(z)). \quad (44)$$

Here we substituted $v_z(z)$ with c , based on the fact that $1/\gamma_z^2 \ll 1$. Eq. (42) is Maxwell's equation in paraxial approximation.

The boundary conditions are taken as in Vainstein [7, 8] as Eq. (23). Since Eq. (23) is valid separately for each component, we can solve Maxwell equations separately for the field along the horizontal and the vertical directions. Independently of the actual shape of \vec{g} , the full problem for a certain polarization component can be written as

$$\begin{cases} \vec{\mathcal{D}}\vec{E}(z, \vec{r}) = g(z, \vec{r}) \\ \left[\vec{E} + (1+i)\beta_0 \sqrt{cb/(4\omega)} (\vec{n} \cdot \vec{\nabla}_{\perp}) \vec{E} \right]_S = 0. \end{cases} \quad (45)$$

We proceed by using a Laplace transform technique, that allows one to dispose of the partial derivative with respect to z in \mathcal{D} in the first equation in (45).

First we define Laplace \mathcal{L} and inverse Laplace \mathcal{L}^{-1} transform of a function $f(z, \vec{r})$ as

$$\widehat{f}(p, \vec{r}) \equiv \mathcal{L}[f(z, \vec{r})](p) = \int_0^{\infty} f(z, \vec{r}) \exp[-pz] dz \quad (46)$$

⁸ Here and everywhere in this paper we make consistent use of Gaussian units.

with $\text{Re}[p] > 0$, and

$$f(z, \vec{r}) \equiv \mathcal{L}^{-1} [\widehat{f}(p, \vec{r})] (z) = \int_{\delta-i\infty}^{\delta+i\infty} \widehat{f}(p, \vec{r}) \exp [pz] dp , \quad (47)$$

where δ is a real number larger than all the real parts of the singularities of $\widehat{f}(p)$.

Consistently applying a Laplace transformation to the equation set (45) we obtain a redefinition of the problem in terms of the Laplace transform of the field $\widehat{E}(p, \vec{r}) \equiv \mathcal{L} [\widetilde{E}(z, \vec{r})] (p)$:

$$\begin{cases} \widehat{\mathcal{D}}\widehat{E}(p, \vec{r}) = \widehat{g}(p, \vec{r}) + \frac{2i\omega}{c}\widetilde{E}(0, \vec{r}) \\ \left[\widehat{E} + (1+i)\beta_0 \sqrt{cb/(4\omega)} (\vec{n} \cdot \vec{\nabla}_\perp) \widehat{E} \right]_S = 0 \end{cases} , \quad (48)$$

where \widehat{g} is the Laplace transform of g and

$$\widehat{\mathcal{D}} \equiv \left(\nabla_\perp^2 + \frac{2i\omega p}{c} \right) . \quad (49)$$

Note that the presence of the initial condition $\widetilde{E}(0, \vec{r})$ in Eq. (48) refers to the possibility of introducing an external field into the system. In what follows⁹ we set $\widetilde{E}(0, \vec{r}) = 0$.

Now, suppose that we find a scalar function \widehat{G} such that

$$\widehat{E} = \int \widehat{G}(\vec{r}, \vec{r}', p) \widehat{g}(\vec{r}', p) d\vec{r}' . \quad (50)$$

In this case, the inverse Laplace transform of \widehat{G} , that will be simply written as G , is the Green's function for the problem (45), inclusive of the proper boundary conditions. As a result

$$\widetilde{E}(\vec{r}, z) = \int_0^z dz' \int d\vec{r}' G(\vec{r}, \vec{r}', z - z') g(\vec{r}', z') , \quad (51)$$

⁹ In our case of interest we have an edge radiation screen at $z = 0$, and at the position immediately behind the screen the field of an electron is equal to zero.

where we integrate up to $z' = z$ because the radiation formation length for $z - z' < 0$ is very short with respect to the case $z - z' > 0$. Summing up, we first have to find \widehat{G} , then to apply a Laplace inverse transform in order to get G and, finally, to solve for \vec{E} .

We start by specifying the eigenvalue problem associated with the problem set (48), that is

$$\begin{cases} \widehat{\mathcal{D}}F_j(\vec{r}) = \Lambda_j F_j(\vec{r}) \\ \left[F_j + (1+i)\beta_0 \sqrt{cb/(4\omega)} (\vec{n} \cdot \vec{\nabla}_\perp) F_j \right]_S = 0 \end{cases} \quad (52)$$

Setting by definition $\lambda_j \equiv 2i\omega p/c - \Lambda_j$ yields the following, equivalent eigenvalue problem:

$$\begin{cases} \nabla_\perp^2 F_j(\vec{r}) + \lambda_j F_j(\vec{r}) = 0 \\ \left[F_j + (1+i)\beta_0 \sqrt{cb/(4\omega)} (\vec{n} \cdot \vec{\nabla}_\perp) F_j \right]_S = 0 \end{cases} \quad (53)$$

Boundary conditions are homogeneous, so that the domain of the Laplacian operator is the vector space of twice differentiable (square integrable) functions obeying boundary conditions in (53). However, the Laplacian operator defined in this way is not self-adjoint with respect to the usual inner product definition, $\langle f, g \rangle \equiv \int_S d\vec{r} f^* g$. This is a result of the fact that the boundary condition in Eq. (53) are not real. Then, eigenvalues are not real, nor eigenfunctions are orthogonal with respect to the usual inner product definition. In general we do not know whether the spectrum is discrete, completeness is not granted and we cannot prove the existence of a set of eigenfunctions either. Yet, direct calculations show that

$$\langle F_j, F_i \rangle = \int_S F_j \cdot F_i d\vec{r}_\perp = \delta_{ji} \quad (54)$$

It follows that functions F_j form a bi-orthogonal set of eigenfunctions. This allows us to decompose \widehat{G} as

$$\widehat{G} = \sum_j \frac{F_j F_j}{2i\omega p/c - \lambda_j} \quad (55)$$

similarly as for a Sturm-Liouville problem. Note that now eigenvalues and eigenfunctions are complex. Also note that the dependence of \widehat{G} on p is at the denominator in Eq. (55). As a result, \widehat{G} goes to zero uniformly as $p \rightarrow \infty$.

It follows that the Mellin transform of \widehat{G} , that is the Green's function G , can be found with the help of Jordan's lemma and reads:

$$G = \sum_j \left\{ \text{Res} \left[\widehat{G} \exp(p_j z) \right] \right\} \quad (56)$$

where

$$\begin{aligned} \left(\text{Res} \left[\widehat{G} \exp[p_j z] \right] \right) &= \lim_{p \rightarrow -ic\lambda_j/(2\omega)} \left\{ \left(p + \frac{ic\lambda_j}{2\omega} \right) \widehat{G}(p) \exp[p_j z] \right\} \\ &= \frac{c}{2i\omega} F_j(\vec{r}) F_j(\vec{r}') \exp \left[-\frac{ic\lambda_j}{2\omega} z \right] \end{aligned} \quad (57)$$

One therefore obtains the following expression for G :

$$G = \sum_j \frac{c}{2i\omega} F_j(\vec{r}) F_j(\vec{r}') \exp \left[-\frac{ic\lambda_j}{2\omega} z \right]. \quad (58)$$

Given the symmetry of the problem we now introduce polar coordinates (r, ϕ) , define $\Delta \equiv (1+i)\beta_0 \sqrt{cb/(4\omega a^2)}$ and rewrite Eq. (53) as

$$\begin{cases} \left(\frac{\partial^2}{\partial r^2} + \frac{1}{r} \frac{\partial}{\partial r} + \frac{1}{r^2} \frac{\partial^2}{\partial \phi^2} \right) F_j(r, \phi) + \lambda_j F_j(r, \phi) = 0 \\ \left[F_j + a\Delta \partial_r F_j \right]_{r=a} = 0 \end{cases}. \quad (59)$$

Posing $j \equiv \{n, k\}$, we look for solutions of Eq. (59) of the form

$$F_{j \equiv \{n, k\}} = f_{nk} \exp(-in\phi), \quad (60)$$

yielding naturally

$$F_{j \equiv \{n, k\}} = A_{nk} J_n(\sqrt{\lambda_{nk}} r) \exp(-in\phi), \quad (61)$$

with

$$J_n(\sqrt{\lambda_{nk}} a) + a\Delta \sqrt{\lambda_{nk}} J'_n(\sqrt{\lambda_{nk}} a) = 0, \quad (62)$$

where J'_n indicates the first derivative of the Bessel function of the first kind of order, J_n , with respect to the argument. Assuming a large Fresnel number $N \equiv a^2/(\lambda b) \gg 1$, which also implies $|\Delta| \ll 1$, one can solve Eq. (62) for λ_{nk} and find

$$\lambda_{nk} = \frac{v_{nk}^2}{a^2}(1 - \Delta)^2 \simeq \frac{v_{nk}^2}{a^2}(1 - 2\Delta), \quad (63)$$

where v_{nk} is the k -th zero of J_n , that is $J_n(v_{nk}) = 0$ for $k = 1, 2, 3, \dots$.

Normalization according to the product in Eq. (54), $\langle F_i, F_j \rangle = \delta_{ij}$ finally yields

$$A_{nk}^2 \simeq \frac{1 - 2\Delta}{\pi a^2 J_{n+1}^2(v_{nk})}. \quad (64)$$

The following, final expression for the Green's function G follows:

$$G = -\frac{ic(1 - 2\Delta)}{2\pi\omega a^2} \sum_{n=-\infty}^{\infty} \sum_{k=1}^{\infty} \frac{\exp[-in(\phi - \phi')]}{J_{n+1}^2(v_{nk})} \exp\left(-\frac{ic(z - z')v_{nk}^2(1 - 2\Delta)}{2\omega a^2}\right) \\ \times J_n\left(\frac{v_{nk}}{a}(1 - \Delta)r\right) J_n\left(\frac{v_{nk}}{a}(1 - \Delta)r'\right). \quad (65)$$

It can be shown that Eq. (65) is in agreement with the findings in [23], where a decomposition of the field in azimuthal components is proposed, and a Green's function is obtained for each azimuthal component following a different reasoning. Eq. (65) can now be used to find the slowly varying amplitude of the field along any given polarization component according to Eq. (51).

In order to verify the correctness of Eq. (65) we study the free-space limit, that corresponds to the limit for large values of the iris radius $a \rightarrow \infty$.

Since we are interested in characterizing the fields over a finite transverse direction, and since sources have a finite transverse size, the limit $a \rightarrow \infty$ allows one to substitute Bessel functions in Eq. (65) with asymptotic expressions for $k \gg 1$. First remember that

$$J_n(\zeta) \approx \sqrt{\frac{2}{\pi\zeta}} \cos\left(\zeta - \frac{\pi n}{2} - \frac{\pi}{4}\right), \quad \zeta \gg 1. \quad (66)$$

One sees that

$$v_{nk} = \pi\left(\frac{n}{2} + k + \frac{3}{4}\right), \quad (67)$$

yielding

$$J_{n+1}^2(v_{nk}) \simeq \frac{2}{\pi v_{nk}}. \quad (68)$$

Substituting Eq. (68) in Eq. (65), posing $\xi = \pi k/a$ and replacing the sum over k in Eq. (65) with an integral over $d\xi$ we obtain:

$$G(r, r', \phi - \phi', z - z') = \frac{c}{4i\omega\pi} \sum_{n=-\infty}^{\infty} \int_0^{\infty} d\xi \xi \exp\left[-\frac{ic(z-z')}{2\omega} \xi^2\right] \times J_n(\xi r) J_n(\xi r') \exp[-in(\phi - \phi')]. \quad (69)$$

Eq. (69) can also be written as

$$G(r, r', \phi - \phi', z - z') = \frac{c}{4i\omega\pi} \int_0^{\infty} d\xi \xi \exp\left[-\frac{ic(z-z')}{2\omega} \xi^2\right] \times J_0(\xi r) J_0(\xi r') + \frac{c}{2i\omega\pi} \sum_{n=1}^{\infty} \int_0^{\infty} d\xi \xi \exp\left[-\frac{ic(z-z')}{2\omega} \xi^2\right] \times J_n(\xi r) J_n(\xi r') \cos[n(\phi - \phi')]. \quad (70)$$

Here $z > z'$. The integrals in $d\xi$ can be performed yielding

$$G(r, r', \phi - \phi', z - z') = -\frac{1}{4\pi(z-z')} J_0\left(\frac{\omega r r'}{c(z-z')}\right) \times \exp\left[\frac{i(r^2 + r'^2)\omega}{2c(z-z')}\right] - \frac{1}{2\pi} \sum_{n=1}^{\infty} i^{-n} J_n\left(\frac{\omega r r'}{c(z-z')}\right) \times \exp\left[\frac{i(r^2 + r'^2)\omega}{2c(z-z')}\right] \cos[n(\phi - \phi')]. \quad (71)$$

Using the Anger-Jacobi expansion

$$J_0(\zeta) + 2 \sum_{n=1}^{\infty} i^{-n} J_n(\zeta) \cos[n(\phi - \phi')] = \exp[-i\zeta \cos(\phi - \phi')] \quad (72)$$

we find that in free-space the Green's function Eq. (65) reduces to

$$G = -\frac{1}{4\pi(z-z')} \exp\left[i\omega \frac{|\vec{r} - \vec{r}'|^2}{2c(z-z')}\right], \quad (73)$$

as it must be.

5 Edge radiation in an iris line

Let us consider the case of an electron emitting edge radiation in an iris line. The vector \vec{g} , whose horizontal and vertical components are needed in order to find the field according to Eq. (51) can be written as

$$\vec{g} = -\frac{4\pi e}{c} \exp\left(\frac{i\omega z'}{2c\gamma^2}\right) \vec{\nabla}_\perp \delta(\vec{r}) . \quad (74)$$

After integrating Eq. (51) by parts, the horizontal and vertical polarization components of \vec{E} turn out to be given by

$$\vec{E}_{x,y} = \frac{4\pi e}{c} \int_{-L/2}^{L/2} dz' \exp\left(\frac{i\omega z'}{2c\gamma^2}\right) \int d\vec{r}' \partial_{x',y'} G(\vec{r}, \vec{r}', z - z') \delta(\vec{r}') , \quad (75)$$

where the choice of the integration limits implies that the reference system now has its origin in the center of the drift between the two edges. Since in Eq. (65) the Green's function is expressed in terms of polar coordinates, we express likewise the partial derivatives with respect to x' and y' as

$$\partial_{x'} = \cos(\phi') \partial_{r'} - \frac{\sin(\phi')}{r'} \partial_{\phi'} \quad (76)$$

and

$$\partial_{y'} = \sin(\phi') \partial_{r'} - \frac{\cos(\phi')}{r'} \partial_{\phi'} . \quad (77)$$

Note that one can transform the partial derivative with respect to y' to that with respect to x' by just substituting $\cos(\phi')$ with $\sin(\phi')$, and $\sin(\phi')$ with $-\cos(\phi')$. Remembering that $\delta(\vec{r}') = \delta(r')/(\pi r')$, using

$$\int_0^{2\pi} d\phi' \exp(-in\phi') \cos(\phi') = \pi \text{ for } n = \pm 1, \text{ and } 0 \text{ otherwise} , \quad (78)$$

$$\int_0^{2\pi} d\phi' \exp(-in\phi') \sin(\phi') = \pm\pi/i \text{ for } n = \pm 1, \text{ and } 0 \text{ otherwise} , \quad (79)$$

$$\lim_{r' \rightarrow 0} J'_{\pm 1} \left(\frac{v_{1k}(1-\Delta)r'}{a} \right) = \lim_{r' \rightarrow 0} \frac{J_{\pm 1} \left(\frac{v_{1k}(1-\Delta)r'}{a} \right)}{r'} = \pm \frac{v_{1k}(1-\Delta)}{2a}, \quad (80)$$

and remembering that $v_{nk} = v_{-nk}$, $J_0^2(v_{1k}) = J_2^2(v_{-1k})$ and $J_1(x) = -J_{-1}(x)$ one finds the following expression for the field at the mirror position:

$$\begin{aligned} \widetilde{E}_x(r, \phi) = & -\frac{2ie(1-\Delta)(1-2\Delta)L \cos(\phi)}{\omega} \sum_{k=1}^{\infty} \frac{v_{1k} J_1(v_{1k}(1-\Delta)r/a)}{a^3 J_0^2(v_{1k})} \\ & \times \text{sinc} \left[\left(\frac{\omega}{2c\gamma^2} + \frac{cv_{1k}^2(1-2\Delta)}{2\omega a^2} \right) \frac{L}{2} \right] \exp \left(-\frac{icv_{1k}^2(1-2\Delta)L}{2\omega a^2} \frac{L}{2} \right) \end{aligned} \quad (81)$$

for the horizontal component and

$$\begin{aligned} \widetilde{E}_y(r, \phi) = & -\frac{2ie(1-\Delta)(1-2\Delta)L \sin(\phi)}{\omega} \sum_{k=1}^{\infty} \frac{v_{1k} J_1(v_{1k}(1-\Delta)r/a)}{a^3 J_0^2(v_{1k})} \\ & \times \text{sinc} \left[\left(\frac{\omega}{2c\gamma^2} + \frac{cv_{1k}^2(1-2\Delta)}{2\omega a^2} \right) \frac{L}{2} \right] \exp \left(-\frac{icv_{1k}^2(1-2\Delta)L}{2\omega a^2} \frac{L}{2} \right) \end{aligned} \quad (82)$$

for the vertical one.

Eq. (81) and Eq. (82) can be used as a basis to calculate the energy per unit spectral interval per unit surface at the sample position. In our case of interest, the distance between sample and extracting mirror, L_s , is much longer compared with the length of the edge radiation setup. Assuming $L_s \gg L$ and accounting for coherence through the form factor $\bar{F}(\omega)$ the field energy per unit spectral interval per unit surface at the sample position is given by

$$\begin{aligned} \frac{dW}{d\omega dS} = & \frac{c}{4\pi^2} N_e^2 |\bar{F}(\omega)|^2 \left| \widetilde{E} \right|^2 \\ = & \frac{4e^2 L^2 c}{4\pi^2 a^6 \omega^2} N_e^2 |\bar{F}(\omega)|^2 \sum_{k=1}^{\infty} \frac{v_{1k}^2}{J_0^4(v_{1k})} \exp \left(-\frac{v_{1k}^2 \beta_0 c^{3/2} b^{1/2}}{\omega^{3/2} a^3} L_s \right) \\ & \times \text{sinc}^2 \left[\frac{L}{4} \left(\frac{\omega}{c\gamma^2} + \frac{v_{1k}^2 c}{\omega a^2} \right) \right] J_1^2 \left(\frac{v_{1k} r}{a} \right). \end{aligned} \quad (83)$$

It should be noted that in the calculation of the square modulus of the field, $\left| \widetilde{E} \right|^2$, crossed terms with different values of k vanish. Integrating over transverse coordinates over the iris hole, and assuming $\Delta\omega/\omega \ll 1$ small enough to neglect the dependence on ω in Eq. (83) one finds the energy of the radiation pulse as

$$W = \frac{e^2 L^2 c}{\pi \omega a^4} N_e^2 |\bar{F}(\omega)|^2 \sum_{k=1}^{\infty} \frac{v_{1k}^2}{J_0^2(v_{1k})} \exp\left(-\frac{v_{1k}^2 \beta_0 c^{3/2} b^{1/2}}{\omega^{3/2} a^3} L_s\right) \times \text{sinc}^2 \left[\frac{L}{4} \left(\frac{\omega}{c\gamma^2} + \frac{v_{1k}^2 c}{\omega a^2} \right) \right] \frac{\Delta\omega}{\omega} . \quad (84)$$

For the THz wavelength range and for the XFEL spent electron beam energies, the constant $L\omega/(c\gamma^2) \ll 1$ and can be neglected in all cases of interest.

6 Radiation of an electron wiggling in an iris line

Let us now consider the case of an electron emitting radiation from a planar undulator with period λ_w in an iris line. We will be interested in frequencies near the fundamental harmonic $\omega_r = 2k_w c \bar{\gamma}_z^2$, where $\bar{\gamma}_z = \gamma / \sqrt{1 + K^2/2}$, $k_w = 2\pi/\lambda_w$ and K is the undulator parameter. We can specify "how near" the frequency of interest ω is compared to ω_r by introducing a detuning parameter C defined as

$$C = \frac{\Delta\omega}{\omega_r} k_w , \quad (85)$$

where $\Delta\omega = \omega - \omega_r$. It can be shown that within the limit

$$|C| \ll k_w , \quad (86)$$

many simplification arise and we can neglect all non-resonant components in Maxwell equations. This amounts to neglecting the gradient component in the vector \vec{g} , and to neglecting the constrained motion $\vec{r}(z)$ in the Dirac δ -function, that is, effectively, in the Green's function. Following these prescriptions, \vec{g} can be written as

$$\vec{g} = -\frac{4\pi e}{c} \exp \left[i \int_0^z d\bar{z} \frac{\omega}{2\gamma_z^2(\bar{z})c} \right] \frac{i\omega}{c^2} v_x(z) \delta(\vec{r}) \vec{e}_x . \quad (87)$$

Eq. (51) yields the following expression for the horizontal field component \bar{E} :

$$\bar{E} = \frac{e\omega\theta_s A_{JJ}}{c^2} \int_{-L_w/2}^{L_w/2} dz' \exp(iCz') \int_0^a dr' \int_0^{2\pi} d\phi' G(r, r', \phi, \phi', z - z') \delta(r') , \quad (88)$$

where $\theta_s = K/\gamma$, L_w is the undulator length and $A_{JJ} = J_0[K^2/(4 + 2K^2)] - J_1[K^2/(4 + 2K^2)]$. Inspection of Eq. (65) shows that only the term with $n = 0$ yields non-zero contributions. One therefore obtains the following azimuthal-symmetric expression for the field at the exit of the undulator:

$$\begin{aligned} \tilde{E}(r) = & -\frac{i(1-2\Delta)e\theta_s A_{JJ}}{ca^2} \sum_{k=1}^{\infty} \frac{1}{J_1^2(\nu_{0k})} J_0\left(\frac{\nu_{0k}}{R}(1-\Delta)r\right) \exp\left(-\frac{ic\nu_{0k}^2(1-2\Delta)L_w}{2\omega a^2}\right) \\ & \times \int_{-L_w/2}^{L_w/2} dz' \exp(iCz') \exp\left(\frac{ic\nu_{0k}^2(1-2\Delta)z'}{2\omega a^2}\right). \end{aligned} \quad (89)$$

Performing the integration in dz' finally yields

$$\begin{aligned} \tilde{E}(r) = & -\frac{i(1-2\Delta)e\theta_s A_{JJ}}{ca^2} \sum_{k=1}^{\infty} \frac{1}{J_1^2(\nu_{0k})} J_0\left(\frac{\nu_{0k}}{R}(1-\Delta)r\right) \exp\left(-\frac{ic\nu_{0k}^2(1-2\Delta)L_w}{2\omega a^2}\right) \\ & \times L_w \text{sinc}\left[\frac{L_w}{2}\left(C + \frac{c\nu_{0k}^2(1-2\Delta)}{2\omega a^2}\right)\right]. \end{aligned} \quad (90)$$

Eq. (90) can be used as a basis to calculate the energy per unit spectral interval per unit surface at the sample position. In our case of interest, the distance between sample and extracting mirror, L_s , is much longer compared with the length of the undulator. Assuming $L_s \gg L_w$ and accounting for coherence through the form factor $\bar{F}(\omega)$, the field energy per unit spectral interval per unit surface at the sample position is given by

$$\begin{aligned} \frac{dW}{d\omega dS} = & \frac{c}{4\pi^2} N_e^2 |\bar{F}(\omega)|^2 \left| \tilde{E} \right|^2 \\ = & \frac{e^2 L_w^2 \theta_s^2 A_{JJ}^2}{4\pi^2 ca^4} N_e^2 |\bar{F}(\omega)|^2 \sum_{k=1}^{\infty} \frac{1}{J_1^4(\nu_{0k})} \exp\left(-\frac{\nu_{0k}^2 \beta_0 c^{3/2} b^{1/2}}{\omega^{3/2} a^3} L_s\right) \\ & \times \text{sinc}^2\left[\frac{L_w}{2}\left(C + \frac{c\nu_{0k}^2}{2a^2\omega}\right)\right] J_0^2\left(\nu_{0k} \frac{r}{a}\right), \end{aligned} \quad (91)$$

It should be noted that in the calculation of the square modulus of the field, $|\tilde{E}|^2$, crossed terms with different values of k vanish. Integrating over transverse coordinates over the iris hole, and assuming $\Delta\omega/\omega \sim 1/N_w \ll 1$ small enough to neglect the dependence on ω in Eq. (91) one finds the energy per spectral interval $\Delta\omega/\omega$ as

$$W = \frac{e^2 L_w^2 \omega \theta_s^2 A_{JJ}^2}{4\pi ca^2} N_e^2 |\bar{F}(\omega)|^2 \sum_{k=1}^{\infty} \frac{1}{J_1^2(\nu_{0k})} \exp\left(-\frac{\nu_{0k}^2 \beta_0 c^{3/2} b^{1/2}}{\omega^{3/2} a^3} L_s\right)$$

$$\times \text{sinc}^2 \left[\frac{L_w}{2} \left(C + \frac{cv_{0k}^2}{2a^2\omega} \right) \right] \frac{\Delta\omega}{\omega}. \quad (92)$$

As expected, different modes do not interfere. The total pulse energy is given by the sum of the energy of each of the empty iris guide eigenmode excited within the open waveguide.

One figure of merit of interest is the ratio between the pulse energy generated and transported within the iris guide, and the pulse energy generated and transported in free space. In the space-frequency domain, the field distribution from the undulator in free space is easily derived. One should take the limit for $a \rightarrow \infty$ in Eq. (88). Accounting for Eq. (73), we get the following well-known expression in the far zone limit (i.e. for $z \gg L_w$):

$$\vec{E}_\perp(z, \vec{\theta}) = -\frac{\theta_s \omega e L_w A_{JJ}}{2c^2 z} \exp \left[i \frac{\omega \theta^2 z}{2c} \right] \text{sinc} \left[\frac{L_w}{2} \left(C + \frac{\omega \theta^2}{2c} \right) \right] \vec{e}_x, \quad (93)$$

where $\vec{\theta} = \vec{r}/z$ defines the observation direction, and $\theta = |\vec{\theta}|$. The distribution of energy radiated per unit solid angle, per unit frequency interval is defined as

$$\frac{dW}{d\omega d\Omega} = \frac{cz^2}{4\pi^2} N_e^2 |\bar{F}(\omega)|^2 \left| \frac{\vec{z}}{E} \right|^2. \quad (94)$$

Integration over angles can be easily performed leading to

$$W_{fs} = \frac{e^2 L_w \omega^2 \theta_s^2 A_{JJ}^2}{8c^2} N_e^2 |\bar{F}(\omega)|^2 \frac{\Delta\omega}{\omega}. \quad (95)$$

This expression corresponds to the particular choice of detuning parameter $C = 0$, at which the pulse energy (in free space) achieves its maximum. The ratio between the energy of the pulse generated and transmitted with quasi-optical techniques and that of the pulse generated and transmitted in free space provides a measure of the departure from ideal performance. Accounting for Eq. (32), Eq. (92), and Eq (95) we get the following expression for this ratio:

$$\begin{aligned} \frac{W}{W_{fs}} &= \frac{2}{\pi} \frac{c L_w}{\omega a^2} \sum_{k=1}^{\infty} \frac{1}{J_1^2(\nu_{0k})} \exp \left[-\frac{\nu_{0k}^2 \beta_0 c^{3/2} b^{1/2}}{\omega^{3/2} a^3} L_s \right] \\ &\times \text{sinc}^2 \left[\frac{L_w}{2} \left(C + \frac{cv_{0k}^2}{2a^2\omega} \right) \right]. \end{aligned} \quad (96)$$

THz radiation source at the LCLS baseline

phase I THz edge radiation source

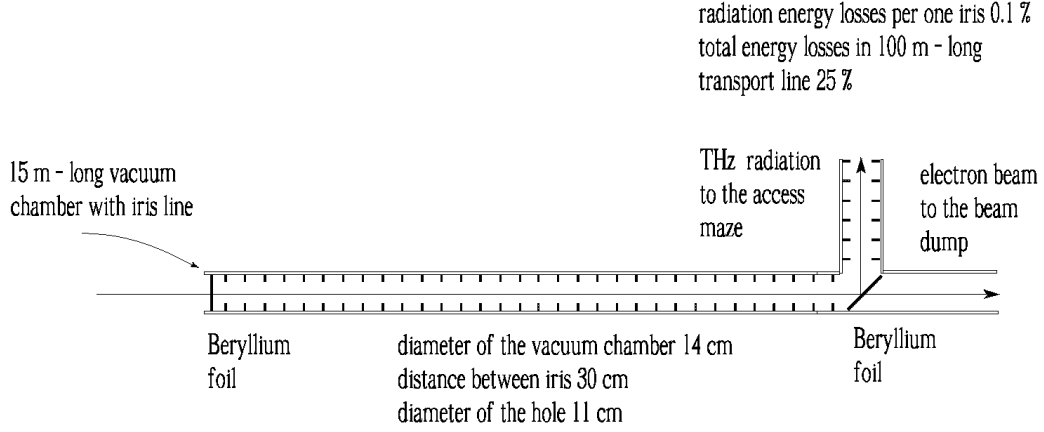


Fig. 23. Scheme of generation of edge radiation at the LCLS baseline.

THz edge radiation source

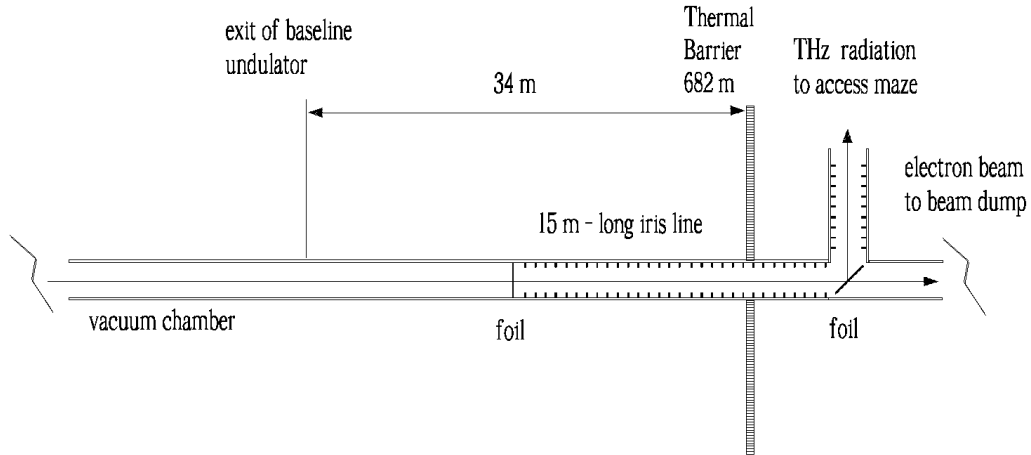


Fig. 24. Installation of the iris line for the THz edge radiation source downstream of the LCLS baseline undulator.

7 Scheme for generating THz edge radiation from the LCLS baseline

The THz edge radiation source proposed in this paper is compatible with the layout of the LCLS baseline and can be realized with minimal additional efforts. The vacuum chamber equipped with iris line and outcoupling system can be installed in the unoccupied straight vacuum line behind the baseline undulator, Fig. 23 and Fig. 24. The transport of the THz beam in

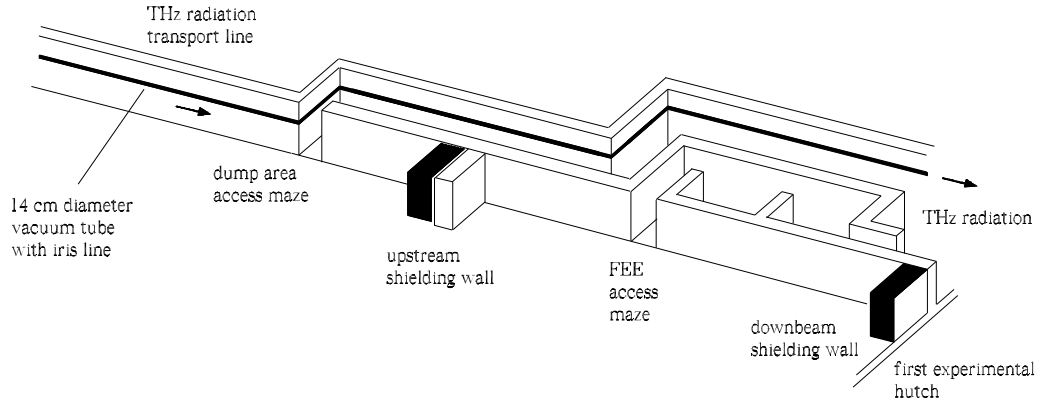


Fig. 25. Scheme of transport of the THz radiation to the experimental X- ray floor.

double electron bunch generation for THz pump - X-ray probe experiments at the LCLS baseline

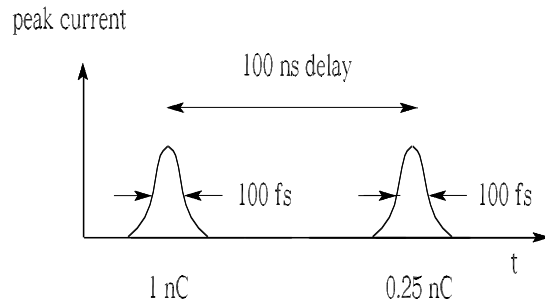


Fig. 26. Double electron bunch generation for THz pump/X-ray probe experiments at the LCLS. The THz radiation transport through the access maze introduces a path delay with respect to the X-ray path, which has to be compensated with the introduction of a delay between two bunches.

the LCLS baseline case only be done with the use of the dump area access maze, which is reproduced schematically in Fig. 25.

The THz transmission line transporting the THz radiation through the access maze introduces a path-delay of about 30 m. Since THz pump/X-ray probe experiments should be enabled, we propose to exploit a two-bunch

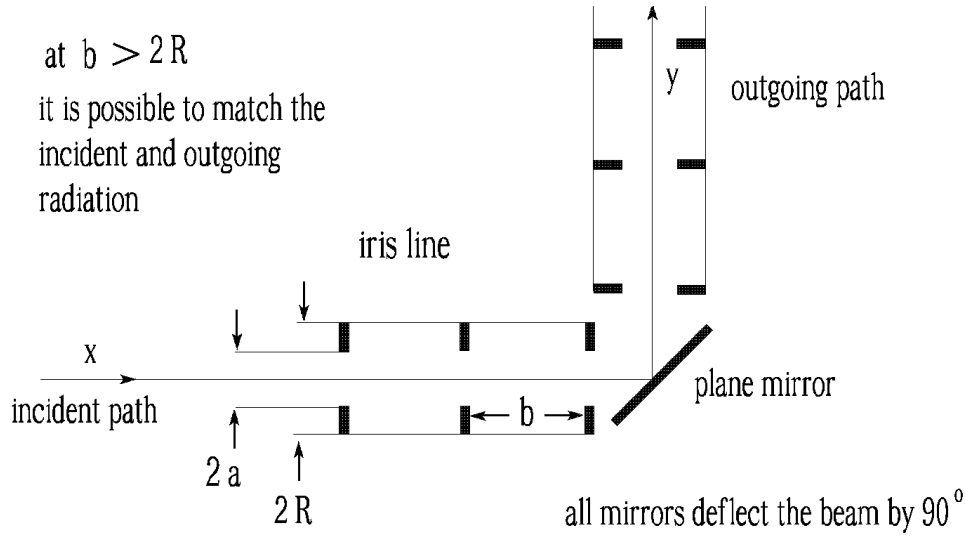


Fig. 27. Geometry of the transmission line turn. The losses are calculated at the wavelength $\lambda = 0.1$ mm.

mode of operation in order to cope with the delay between THz and X-ray pulses, Fig. 26. The two bunches should be precisely separated by a certain temporal delay and such delay should be matched to that introduced by the THz transmission line. The main idea is, first, to produce two electron bunches at a fixed distance with respect to each other. Second, the bunches are accelerated and compressed. The beam energy and position is kept nearly identical, while they progress one after the other through the undulator and THz setup. A way to create two pulses delayed with respect to each other is to split the UV laser pulse which illuminates the cathode, delay one of the pulses, and then recombine the pulses on the same trajectory heading towards the rf gun. One method for accomplishing this is described in [22, 24]. A multibunch mode of operation was also used at the SLAC linac [25]. Routine operation with about 60 ns spacing was achieved. It should be noted that for the present scheme (in contrast with that discussed in [22]) we do not require an essentially flat RF amplitude between bunches.

The operation of the proposed THz source is insensitive to the emittance and energy spread of the electron beam. An analysis of the parameters of the THz source shows that it will operate reliably even for emittance and energy spread exceeding the LCLS commissioning results by an order of magnitude.

The THz transmission line for the LCLS baseline includes at least six 90 degrees turns, and will exploit plane mirrors as functional components. If the pipe of the transmission line has a diameter smaller than the distance between the irises it is possible to match incident and outgoing radiation

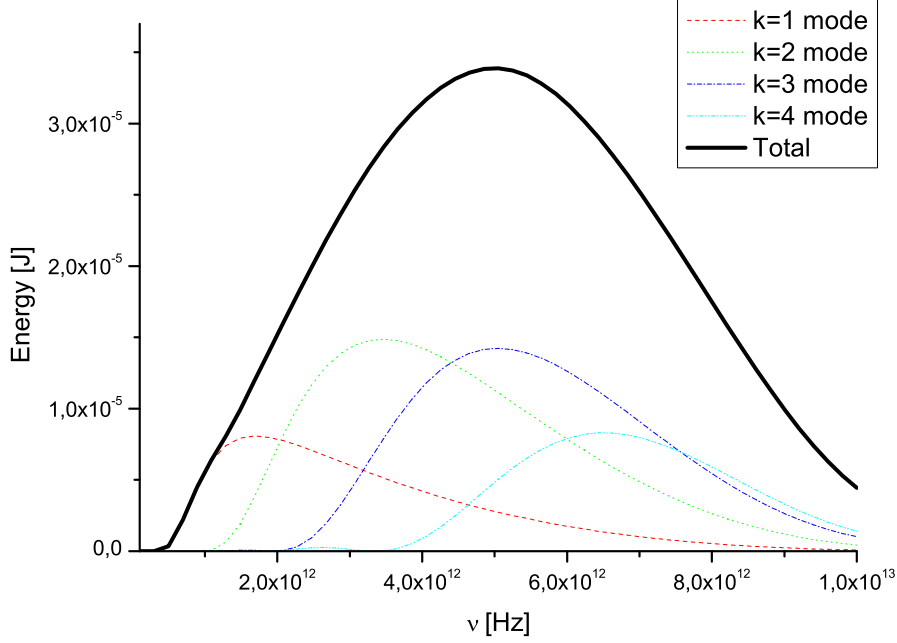


Fig. 28. Edge radiation pulse energy emitted within spectral bandwidth $\Delta\omega/\omega = 10\%$ and transported at the sample position as a function of frequency. Partial contributions of individual modes of the circular iris guide are illustrated. The sample is set 100 meters away from the extracting mirror. The curves are calculated with analytical formulas in Eq. (32) and Eq. (84). Here $N_e = 6.4 \cdot 10^9$ (1 nC), $L = 15$ m, $b = 30$ cm, $2a = 11$ cm. The bunch form factor used is shown in Fig. 7.

without extra losses in these irregularities, Fig. 27.

It is possible to calculate the energy in the pulse, assuming a 10% spectral bandwidth. The bunch form factor considered here is given in Fig. 7. We also consider a total length of the iris line of 100 m. The energy loss in the line are accounted for. The energy per pulse at the exit of the iris line as a function of the frequency $\nu = \omega/(2\pi)$ is shown in Fig. 28.

The maximal value of the pulse energy is achieved at $\lambda \simeq 0.06$ mm. When the bandpass filter is tuned to this value of λ , the expression for the total edge radiation pulse energy at the sample can be written in the form:

$$W[\text{mJ}] \simeq 0.34 \cdot \frac{\Delta\omega}{\omega}. \quad (97)$$

The energy as a function of frequency exhibits a low frequency cutoff due to losses in the transport line and a high frequency cutoff due to form factor suppression.

THz radiation source at the LCLS baseline

phase II THz undulator source

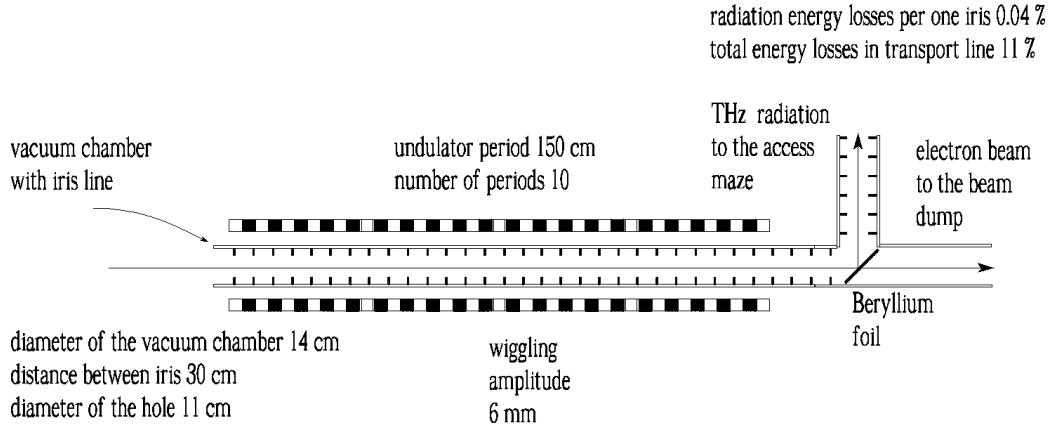


Fig. 29. Scheme for generating THz undulator radiation at the LCLS baseline. The installation of the THz undulator does not perturb the edge radiation setup and does not interfere with the THz edge radiation source operation. The losses are calculated at the wavelength $\lambda = 0.1$ mm.

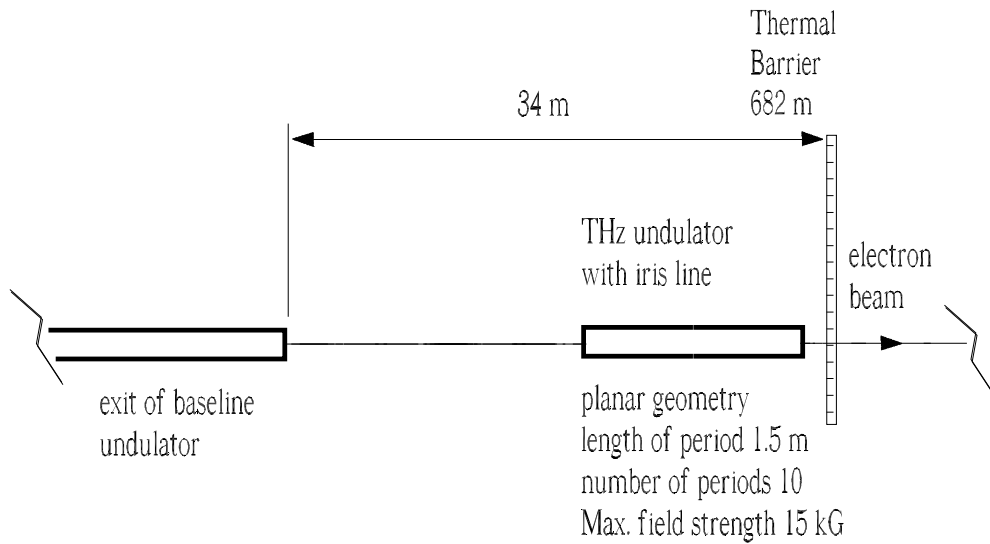


Fig. 30. Installation of the THz undulator downstream of the baseline undulator.

8 Scheme for generating THz undulator radiation from the LCLS baseline

As discussed in Section 2, an optimal expansion strategy for the LCLS THz source should be based on the installation of a THz undulator, Fig. 29,

Fig. 30. The undulator proposed is an inexpensive planar electromagnetic device with 10 periods, each 1.5 m long. At the electron beam energy around 5 GeV and at a THz wavelength around 0.2 mm, the peak value of the magnetic field is about 1.5 T. Undulator radiation will be produced around the fundamental harmonic, and the fundamental harmonic will be tuned by adjusting the magnetic field strength. The wavelength range between 0.05 mm and 0.2 mm provided by this powerful radiation source will overlap with a large part of the THz gap. This will allow applications for pump-probe experiments combining THz and X-ray radiation¹⁰.

Note that in the case of THz undulator source at LCLS the electron beam emittance is much smaller than the radiation wavelength. This means that the electron beam can safely be modeled as filament beam. Computer codes like SRW [26] and SPECTRA [27] can be used to study the characteristics of the output radiation in the space-frequency domain up to a wavelength where the influence of the vacuum chamber is negligible. However, in the case of the THz undulator source at the LCLS, wavelengths of order of 0.1 mm and 15 m - long undulator yield a radiation diffraction size of order of 10 cm. This rough estimate indicates that vacuum chamber effects are expected to play an important role. In this case, conventional computer codes fail to predict the correct radiation characteristics.

Summing up, in view of practical applications to the THz undulator at LCLS, there is a need for a theory of undulator radiation in the presence of a waveguide. In [28] we developed a theory of undulator radiation in the presence of the vacuum chamber with circularly symmetric cross-section. In order to efficiently couple radiation into the iris transmission line, for the LCLS case we proposed to use a THz undulator source together with an iris line, Fig. 29 and Fig. 30. The task that one has to solve differs from the circular vacuum chamber case [28] in the formulation of boundary conditions. Using Leontovich boundary conditions gives a good approximation in the case of a metallic vacuum pipe with resistive walls, and drastically simplifies the solution of the electrodynamical problem [28]. The problem of mode excitation in an iris waveguide can be solved following the same approach, where Leontovich boundary conditions are now substituted by Vainstein boundary conditions. In our practical case of interest the wiggling amplitude of the electrons in the undulator is small with respect to the dimension of the iris waveguide, Fig. 30. This greatly simplifies analytical calculations. In free-space and under the resonance approximation undulator radiation is horizontally polarized. This is actually a replica of the undulator polar-

¹⁰ There is a trade-off between the far-infrared and the X-ray frequency range achievable in the case a THz undulator source is used. For instance, at an electron energy around 10 GeV the longest far-infrared and shortest X-ray wavelengths available for operations are around 0.05 mm and 0.25 nm respectively.

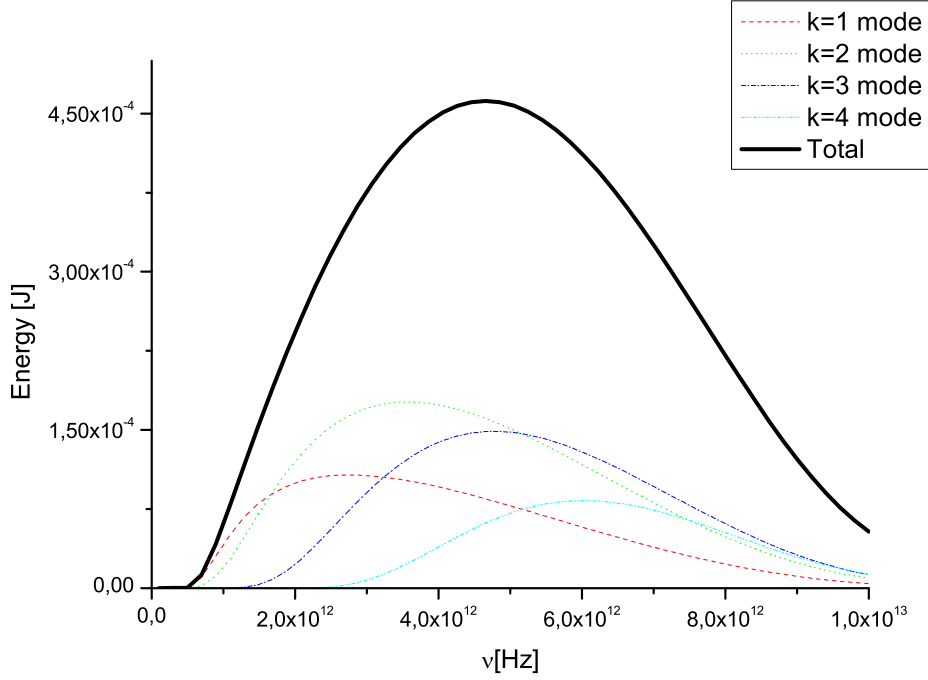


Fig. 31. Undulator radiation pulse energy emitted with a spectral bandwidth $\Delta\omega/\omega = 10\%$ and transported at the sample position as a function of frequency. Partial contributions of individual modes of the circular iris guide are illustrated. The sample is set 100 meters away from the extracting mirror. The curves are calculated with the analytical formulas in Eq. (32) and Eq. (92). Here $N_e = 6.4 \cdot 10^9$ (1 nC), $N_w = 10$, $\lambda_w = 1.5$ m, $b = 30$ cm, $2a = 11$ cm. The bunch form factor used is shown in Fig. 7. Curves correspond to the particular choice of the detuning parameter C at which the pulse energy in the second mode achieves its maximum.

ization properties. Moreover, the field exhibits azimuthal symmetry. This properties are the same when an iris line is introduced ¹¹.

It is possible to calculate the energy in the pulse, assuming a 10% spectral bandwidth. The bunch form factor considered here is given in Fig. 7. We also consider a total length of the iris line of 100 m. The energy loss in the line are also accounted for. The energy per pulse at the exit of the iris line as a function of the frequency $\nu = \omega/(2\pi)$ is shown in Fig. 31.

It can be easily shown that the energy per spectral interval, Eq. (92), does not depend on the energy of the electron beam nor, in our case of interest with $K \gg 1$, on the undulator parameter. In other words, we assume that the fundamental harmonic will be tuned by adjusting the magnetic field strength at some fixed electron beam energy, but there is no need to specify

¹¹ These properties are lost in the case of metallic pipe when Leontovich boundary conditions are introduced [28].

these parameters.

It is instructive to calculate the ratio W/W_{fs} in Eq. (96) and find the departure of the results presented in Fig. 31 from the free space, ideal performance. Calculating the Eq. (96) at the sample position and at the optimal wavelength $\lambda \simeq 0.06$ mm, we obtain $W/W_{fs} \simeq 0.8$. This comparison demonstrates the effectiveness of the proposed setup.

Finally, we note that according to our calculations, at a wavelength around 0.06 mm, and for ten cycles in the pulse, one obtains a 0.3 GW peak power level on the sample (see Fig. 31). With strong focusing, these THz beams will approach the high field limit of 1 V/atomic size.

9 Conclusions

In this paper we presented a design of a THz edge radiation source and a possible extension to a THz undulator radiation source for the LCLS baseline. We began our considerations from the generation of THz radiation from the spent electron beam downstream of the baseline undulator. Transmission of the THz beam can only be accomplished with quasi-optical techniques. In this article we proposed to use an open beam waveguide such as an iris guide, and we presented a complete theory of iris guides. In particular, eigenmodes were studied both numerically and analytically. In order to efficiently couple radiation into the iris transmission line, it is desirable to match the spatial pattern of the source radiation to the propagating mode of the transmission line. To solve the matching problem, we proposed to generate the THz radiation within the iris guide.

Following a derivation of the iris guide Green's function we presented the first exhaustive theory of edge and undulator radiation within an iris guide, and we exemplified it in the case of the proposed THz source at LCLS. We specialized our consideration to the case of a circular iris waveguide. The electric field was found as a superposition of the iris waveguide modes, and was studied for the LCLS parameters case.

The concepts presented here are applicable not only to the LCLS, but also to other XFEL facilities. In fact, we regard the concepts presented here, based on the combination of edge radiation and undulator radiation with an open waveguide setup, as the start of a novel direction towards the construction of THz sources at XFELs. Therefore, the present work should not be considered as comprehensive of all possible solutions. On the contrary, this work is presented with the goal of stimulating interest and of opening the door to new possibilities for THz radiation production and transport at XFELs.

10 Acknowledgements

We are grateful to Massimo Altarelli, Reinhard Brinkmann, Serguei Molodtsov and Edgar Weckert for their support and their interest during the compilation of this work.

References

- [1] The LCLS-II Conceptual design report, https://slacportal.slac.stanford.edu/sites/lcls_public/lcls_ii/Published_Documents/CDR%20Index.pdf
- [2] J. N. Galayda, Z. Huang and P.A. Heimann Proceedings of 2011 PAC, New York, NY, USA, TUOBS1
- [3] Z. Wu, et al., Proceedings of 2011 PAC, New York, NY, USA, MOP071
- [4] S. Moeller et al., Photon beamlines and diagnostics at LCLS Nucl. Instr. and Meth. A , Volume 635, Supplement 1, page S6 (2010).
- [5] M. Santana-Leitner et al., "Commissioning of the Electron Line of the Linac Coherent Light Source Dose Rate Measurements and Simulations", SLAC-PUB-13637 (2009)
- [6] A. G. Fox and T. Li, Bell syst. Tech. J. 40. 453 (1961).
- [7] L. A. Vainstein, "Open resonators for lasers" Sov. Phys. JETP, vol. 17, pp 709-719.
- [8] L. A. Vainstein (also Anglicized as Weinstein), Open Resonators and Open Waveguides, Colem Press, 1969.
- [9] B. Faatz et al., Nucl. Instrum. Meth. A 475, 363 (2001)
- [10] Gensch M. et al., 2008 Infrared phys. Technology. 51 423-5
- [11] P.M. Morse and H. Feshbach Methods of Theoretical Physics (McGraw-Hill, New York, p. 884 (1953)
- [12] G. Goubau and F. Schwing, "On the guided wave propagation of electromagnetic wave beams" IEEE Trans. Microwave Theory Tech., vol. 9, pp. 248-256, Mar. 1961.
- [13] J. E. Christian and G. Goubau, "Some measurements on an iris beam waveguide" Proc. IEEE, vol. 49, pp. 1679-1680, Nov. 1961.
- [14] B. Z. Katsenelenbaum, "Transmission of mm waves by reflection from a series of focusing reflectors" Radio Eng. Electron. Phys., no. 9, p. 1446, 1963
- [15] J. E. Degenford, M. D. Sirkis, and W. H. Steier, "The reflecting beam waveguide" IEEE Trans. Microwave Theory Tech., vol. 12, pp. 445-453, Jul. 1964
- [16] M. Sorolla, R. Martin et al., "Beam waveguide for ECRH at TJ-II" International Journal of Infrared and Millimeter Waves, Vol. 18, No. 6, pp. 1161-1168, 1997
- [17] A. Fernandes et al., "Quasioptical transmission lines for ECRH at TJ-

- II Stellarator" International Journal of Infrared and Millimeter Waves, Vol. 21, no. 12, pp.1945-1957, 2000.
- [18] G. N. Kulipanov et al., Terahertz Science and Technology, Vol. 1, No . 2, pp. 107, June 2008
 - [19] K. Tiedtke et al., New Journal of Physics 11 (2009) 023029
 - [20] G. Geloni et al. NIM A 605,3, 409 (2009) and NIM A 607,2, 470 (2009), and "Theory of edge radiation" DESY 08-118, <http://arxiv.org/abs/0808.1846>.
 - [21] V.L. Ginzburg and I.M. Frank, Soviet Phys. JETP 16. 15 (1946)
 - [22] Y. Ding, Z. Huang and R. Ruth, PRSTAB 13, 060703 (2010)
 - [23] E.L. Saldin, E.A. Schneidmiller and M.V. Yurkov, Nucl. Instrum. Meth. A 393, 312 (1997).
 - [24] O. Grimm et al., in Proceedings of the 10th European Particle Accelerator Conference, Edinburgh, Scotland, 206 (EPS-AG, Edinburgh, Scotland, 2006).
 - [25] J. T. Seeman et al., SLAC Report No. SLAC-Pub-5438, 1991
 - [26] O. Chubar and P. Elleaume, in Proc. of the 6th European Particle Accelerator Conference EPAC98, Stockholm, Sweden, 1177-1179 (1998)
 - [27] T. Tanaka and H. Kitamura, J. Synch. Rad. 8, 1221 (2001)
 - [28] G. Geloni, et al. "Undulator radiation in a waveguide", Nuclear Instruments and Methods in Physics Research Section A: Accelerators, Spectrometers, Detectors and Associated Equipment 584, 219 (2008)